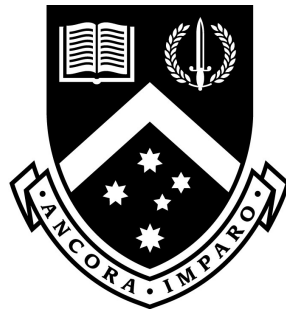# Quantum Plasmonic Analysis of Spasers

Lakshitha Chathuranga Kumarapperuma Arachchige
BSc Eng (Hons)

Submitted in total fulfilment of the requirements for the degree
of
Doctor of Philosophy

Department of Electrical and Computer Systems Engineering
MONASH UNIVERSITY
CLAYTON, AUSTRALIA

March 2020

This page intentionally left blank.

Summary

Device miniaturization and improving the speed of operation are two of the most challenging frontiers that are encountered in electronics. Speed of operation is enhanced by moving into the optical domain for signal processing. However, due to the limit of diffraction in photonics, realizing nanoscale electronic devices still remains a challenge. Spaser (Surface Plasmon Amplification by Stimulated Emission of Radiation) has been introduced as a solution, which opens up a novel branch of nano-electronics and nano-optics which can overcome the existing speed barriers and miniaturization limits simultaneously. Nano-electronics, imaging and bio-optics are some of the potential applications of spasers.

Being the nano-plasmonic counterpart of a laser, a spaser is made by coupling a nano-plasmonic material, acting as a resonator cavity, to a gain medium powered by an incoherent pump. The plasmonic resonator generates localized, intense and coherent electric fields called surface plasmons (SP). Due to the use of conventional two-level gain medium chromophores, many practical limitations have been encountered, in order to experimentally realize highly efficient, low threshold, tunable spasers. Therefore, improving the number of SPs generated per spasing mode to increase the output power, reducing the spasing threshold requirements and integrating tunability are some of the challenging areas of research in spaser design.

This research is intended towards modelling a coherence enhanced spaser with three-level gain medium chromophores, which utilizes an additional coher-

ent optical field with the aim of improving the spaser characteristics. A comprehensive numerical analysis has been performed for the continuous wave operation of a silver nano-sphere spaser, where we demonstrate that coherence enhanced spasing increases the generation of SPs while decreasing the spasing threshold. Moreover, the performance characteristics such as the number of SPs per spasing mode, the behavior of the L-L curve under different conditions, the spasing threshold conditions and the critical pumping requirements are analytically studied. These studies would enable design optimization at an extremely low computational cost whilst providing significant physical insights into the operation of the device. Furthermore, we investigate the interaction of two coherence enhanced 3-level spasers. The transient dynamics as well as the steady state output characteristics are studied both numerically as well as analytically. This study would provide the basis for implementing a network of interacting three-level spasers.

The new knowledge created in this research will be extremely valuable in designing and experimentally realizing optimized, highly efficient spasers which would foster the utilization of spasers in a plethora of nano-plasmonic active structures.

General Declaration

This thesis is an original work of my research and contains no material which has been accepted for the award of any other degree or diploma at any university or equivalent institution and that, to the best of my knowledge and belief, this thesis contains no material previously published or written by another person, except where due reference is made in the text of the thesis.

Signature   :_____

Name   : Lakshitha Chathuranga Kumarapperuma Arachchige

Date   : 5th March 2020

This page intentionally left blank.

Acknowledgements

First and foremost, I would like to extend my sincere appreciation to my supervisor, Prof. Malin Premaratne, for his unsurpassed guidance and encouragement throughout this journey. Without his timely guidance and knowledgeable insights, this thesis would not have been possible.

I would like to thank my colleagues at the Advanced Computing and Simulation Laboratory (AχL) of Monash University (Charith, Dilusha, Chathurangi, Bobo, Ashan, Harini, Sudaraka, Tharindu, Viraj, Dasuni, Champi, Kamani, Nisal, Asha, Tharaka, Ravi, Sachinthana) for continued insightful and encouraging discussions.

I sincerely acknowledge my beloved parents (Srimathi Mallika and Amarapala Kumarapperuma), my loving wife (Lahirunie Kahingala), my brother (Rajitha Mihiranga), my mother-in-law (Padma De Silva) and all my loved ones for the morale support and comfort provided throughout my PhD journey. A special shout out must go to Dr. Harini Hapuarachchi and Dr. Sudaraka Mallawaarachchi for all the insightful discussions and support throughout my PhD journey. There were lots of other friends as well, who made my stay in Melbourne enjoyable. Their presence was mightily helpful in many direct/indirect ways for the success of my thesis. I also hope that my little nephew *Ezra* would someday go through *Laki Maama*'s thesis and suggest some improvements!

I am thankful to the Monash University Institute of Graduate Research and also to the Department of Electrical and Computer Systems Engineering for pro-

To my beloved amma and thaththa, forever loving wife, my mother-in law,

my brother and all tax paying citizens of both Sri Lanka and Australia!

This page intentionally left blank.

Contents

List of Figures

Publications

Published

1. Kumarapperuma L, Premaratne M, Jha PK, Stockman MI and Agrawal GP; "Complete characterization of the spasing (LL) curve of a three-level quantum coherence enhanced spaser for design optimization," Applied Physics Letters, 112(20), (2018).

2. Kumarapperuma L and Premaratne M; "Quantum coherence enhanced graphene spaser," Integrated Photonics Research, Silicon and Nanophotonics 2019, pp. IW2A-5, Optical Society of America, (2019).

Drafted

1. Kumarapperuma L, Stockman MI, Gunapala SD and Premaratne M; "Threshold characteristics of quantum coherence enhanced 3-level spasers," Journal of Physics: Condensed Matter.

This page intentionally left blank.

Chapter 1

Introduction

1.1 Motivation

Ability to manipulate light at the nanoscale at ultrafast speeds enables various different applications through the development of efficient, miniaturized optical circuits and systems. With the evolution of technology in the past few decades, it was evident that faster operating speeds could be achieved using photons, surpassing electrons. Photonics has emerged as a promising technology to address this issue and it has been utilized for designing high speed electronic devices which operate in THz speeds [1]. However, the dimensions in photonic circuits are of the order of micrometers, because the fundamental limit of diffraction has intervened to constrain the miniaturization below the sub wavelength scale [2, 3]. On the other hand, with the advancement of sophisticated nano-fabrication techniques, device sizes approaching tens of nanometers have been designed and manufactured reliably. In essence, light must be confined to unprecedentedly smaller volumes, enabling very strong light-matter interactions [4] to realize nano-scale optical devices. These challenges are predicted to be encountered successfully in the emerging field of quantum nano-plasmonics. It is expected to improve the speed and efficiency of optical devices while facilitating miniaturization beyond the limitations of conventional optoelectronics [5–7].

Quantum nano-plasmonics is a promising active field of research which in-

volves quantum mechanical control of plasmon resonances, development of active plasmonic devices and quantum optical applications using Surface Plasmons (SP) [8,9]. A Surface Plasmon (SP) is a hybrid particle state between electrons and photons [10]. SPs are excited at metal-dielectric interfaces [11]. Therefore they are naturally subjected to intrinsic losses, severely limiting propagation length to a few wavelengths [10, 12]. Consequently, energy must be transferred from an external source to SPs to sustain their existence [3]. A spaser (surface plasmon amplification by stimulated emission of radiation) is the fundamental nano-scale device conceptualized to serve the above purpose by generating and amplifying SPs.

The operating principle of a surface plasmonic laser (i.e. spaser) based on stimulated emission was introduced by Stockman and Bergman in 2003 [13, 14]. Spaser, which is the nano-scale counterpart of a laser, shares many common structural components with a laser. It is made by coupling a nanoparticle (resonator) to an active gain medium . The nanoparticle in a spaser is made of a plasmonic material and it is analogous to the cavity of a macro-level laser. The photons of a laser are replaced by SPs. The optical losses in the plasmonic resonator are compensated by gain in the active medium, generating localized, intense, and coherent optical fields [14–17], similar to the operation of the laser. Spasing occurs due to the nonradiative energy transfer from the gain medium to the resonator, exciting localized SP modes [18–21].

A number of theoretical and experimental work based on spaser are available in literature, including proposals for different device designs [19,22], such as electrically pumped bowtie spaser [23], V-shaped metallic structure surrounded by quantum dots [13], electrically pumped spasers made of silver and gold nanoparticles which work in extreme quantum limits [15] etc. Spasers have been the subject of intensive research in the past few years and it has already been demonstrated that they are well suited for room and low temperature electronics [16,24].

The first experimental implementation of the spaser has been demonstrated us-
ing stimulated emission of SPs in a spherical gold nanoparticle surrounded by
dye-doped silica as the gain medium [18]. There have been several other demon-
strations of the spasing process ever since [10, 25–27].

In addition, coupling between the gain medium and resonators, different types
of gain mediums, geometric and material variations of the nano-plasmonic res-
onator designs have been of special interest among the researchers [28, 29]. These
approaches are aimed at improving the spaser characteristics such as tunability,
plasmon quality factor etc. [16].

However, there are number of practical limitations that must be addressed, for
practically realizing efficient spasers in view of capitalizing from their numerous
promising characteristics. Spasers have comparatively high thresholds which can
hinder the potential applications [30]. In addition, spasers have low efficiencies
where they generate a relatively low number of SPs per spasing mode [4]. Most of
these limitations are caused due to the 2-level gain medium chromophores used
when modelling the spasers, since the gain medium quickly gets saturated due to
the internal plasmonic feedback. An external coherent drive has been introduced
as an additional controlling field to modify the spaser model with a 3-level gain
medium by Dorfman *et al.* recently [31]. A significant increase in the surface
plasmon numbers as well as a significant decrease in the spasing threshold is
reported during numerical simulations.

The effect of additional optical fields and the 3-level model on spaser perfor-
mance needs to be characterized analytically. It will enable extensive research
on using the quantum coherence phenomena to enhance spaser properties. The
behavior of critical output characteristics such as output power and threshold
conditions with the variation of input power and device properties have yet to be
investigated extensively. Such a study will enable the scientists to design devices
to suit different output properties. In addition, interactions of the device with

the operating environment should be modelled with high precision to better describe the operation of spasers. Properties such as decoherence should be taken into consideration in the mathematical models. Furthermore, design optimization guidelines must be established, while generating physical insights. Such an analytical characterization of the operation of the device should be simulated on different spaser set ups for verification. This is what we aspire to achieve in this thesis. Towards the latter part of the research, the interaction of 3-level spasers with external plasmonic fields will be studied, paving way for the design and implementation of spaser arrays. Our overall study will accelerate the use of spasers in a plethora of active nano-plasmonic applications.

This is what we have tried to envisage throughout my PhD research. In brief, the basic objective of this research is to develop a comprehensive analytical and numerical framework to analyze and design coherently enhanced 3-level spasers.

1.2   Aims of research

The general aim of my research is to develop a complete characterization on coherently-enhanced spasers with 3-Level gain medium chromophores to study the improvements of performance parameters of the device such as the output power and spasing threshold while adapting the developed models for analysing various spaser set ups made of different materials and configurations. Our analysis will enhance the practical realization of spasers for various applications. We intend to generate new knowledge through 4 different objectives as described below.

1. **Modelling the spasing (L-L - Light out/Light In) curve of a coherently enhanced 3-level spaser** Apart from the basic numerical simulations that have been conducted, an analytical approach had not been taken in literature to quantify the performance parameters in three-level spasers. If analytical

expressions to characterize the spasing (L-L) curve of a 3-level can be derived, it can be used to characterize the spasing curve, which represents the output power generated by the spaser. The utility of such a solution stems from the fact that it can enable optimization of the large set of parameters associated with spaser designing, a functionality not offered by the methods currently available in literature. This is vital for the advancement of spaser technology towards the level of device realization. Moreover, such an analytical approach will also facilitates the grouping and identification of key processes responsible for spasing action, whilst providing significant physical insights. Additionally, this will drastically reduce the computational cost associated with spaser designing. Therefore, as the first research aim, we intend to analytically characterize the spasing curve with an acceptable accuracy to achieve the above goals.

2. **Threshold characteristics of quantum coherence enhanced 3-level spasers**
   During this stage, we intend to study spasing threshold, which is one of the key output characteristics that require close attention. Given the recent experimental success in demonstrating the operation of the three-level spaser [27], we consider an analytical approach to study the spasing threshold is topical and would enable many promising applications in nano-plasmonics. We plan to derive explicit analytical expressions for population inversions, population densities as well as non-zero off-diagonal terms of the density matrix at spasing threshold. We would then proceed to analytically study the critical pumping rate required to start spasing.

   Such a study will facilitate design optimization of spasers, specially at lower pumping energies. We also plan to obtain simpler expressions, providing better physical insights into the operation of the device. Furthermore, we aim to perform a detailed numerical analysis, quantifying the reduction of critical pumping requirements due to the coherent drive. Such a study

would enable us to explore phenomena such as spasing without inversion in 3-level spasers. Finally, we aspire to scrutinize the effects of decoherence on the spasing threshold for a better understanding of the spaser performance at low power inputs.

3. **A generalized study on the behavior of the output power of 3-level spasers as a framework for design optimization**

   The most common type of spaser model comprises 2-level gain medium chromophores, and a much improved version arises by modelling the gain medium chromophores as 3-level systems. During this stage, as the first step, we plan to obtain an analytical expression for the spasing curve of a two-level spaser, which has not been reported in literature thus far. We intend to use the knowledge we obtain in the previous stages to derive the solution. It would further validate our approach in stage 1 and also provide better physical insights into the operation of spasers in general.

   Furthermore, due to its many perceived advantages such as thermal and chemical stability, mechanical strength and bio-compatibility, graphene has been recently proposed as a potential plasmonic resonator for spasers. We hope to combine the concept of coherence enhanced three-level spasing with a graphene nano-resonator, to design and explore the first three-level graphene spaser, as the next aim of the research. We would further demonstrate the improved characteristics of our design, compared to the conventional 2-level models.

4. **Investigate the dynamics of coherently enhanced 3-level spasers under external plasmonic fields**

   During the initial and middle phases of the research, the Continuous Wave (CW) operation of the spaser will be studied extensively in the steady state regime, with performance enhancement as the basic points of interest. For a

complete study of the spaser characteristics, we would then have to investigate the time evolution and steady state output of the interaction of two such spasers. If we can model the these interactions, it will also enable us to study the effect of external plasmonic fields on the behavior of individual spasers.

The feedback due to back-scattering as well as the effect of the external plasmonic field will be considered in our model. We aim to simulate the initial transients as well as the steady state properties. We believe that such a framework may then be scaled up to study the interaction of many spasers as well, by the careful use of parameters which govern the plasmonic interactions. Since it is predicted that arrays of interacting spasers would be utilized in various promising active plasmonic structures, this final objective of our research, along with the potential knowledge that we plan to obtain in the earlier stages will be of utmost importance for the future applications in nano-plasmonics.

1.3 Thesis outline

Chapter 1 introduces the topic of the research, briefly discussing recent advancements and trends associated with spaser technology. This chapter provides the details of the motivation and the aims, followed by the outline of the thesis.

Chapter 2 presents the background theory of the spaser, including its design and components, how it works, major operational characteristics, and a description on the evolution of spasers. A thorough literature review is presented on theoretical modeling of localized surface plasmons in metal nanoparticles, excitons in quantum emitters and their interactions.

Chapter 3 comprises the fundamental theories and formalism of the spasing phenomena of a 3-level spaser. With a lof of engineering intuition and mathe-

matical insight, an analytical characterization of the number of Surface Plasmons generated per spasing mode has been derived, which represents the power output of a coherently enhanced 3-level spaser. The validation of results demonstrating the accuracy as well as the drastic reduction of computational complexity is presented thereafter. In conclusion, the physical insights that can be derived are also reported along with guidelines for design optimization.

Spasing threshold is another crucial parameter which describes the output characteristics of spasers. With the recent success of experimental realization of a three-level spaser, studying the behaviour of threshold conditions as well as the methods of controlling the threshold characteristics was deemed essential. In chapter 4, we present an analytical approach as well as a detailed numerical simulation to study and control the various physical properties at spasing threshold, as well as the critical pumping requirements.

Chapter 5 provides the much needed basis for spaser design optimization with a sound analytical framework. A generalized study on the behavior of the output power for both 2-level and 3-level spasers will be illustrated, providing significant physical insight. To compliment the study, we analyze a spaser setup made of graphene, demonstrating the improved output characteristics.

In chapter 6, the feedback due to back-scattering as well as the effect of an external plasmonic field have been considered to model the interaction of two spasers made of three-level gain medium chromophores. It provides the much needed basis to study the interaction dynamics of spasers, which would enhance the prospect of using arrays of coherence enhance spasers in active nano-plasmonic systems.

Finally, chapter 7 concludes this thesis by presenting a summary of the major contributions of this research towards the advancement of active plasmonic nano-sources. It will be followed by a discussion of suggested future work to conclude the thesis.

Chapter 2
Theory of spasers

This chapter presents an introduction to the basic components of a spaser, over-arching principles, the evolution of the technology and potential applications in the form of a literature survey.

2.1 Surface Plasmon Amplification by Stimulated Emission of Radiation

2.1.1 Surface Plasmons

A single quanta of the electromagnetic field generated due to the coherent oscillations of electrons on metal-dielectric surfaces can be represented by one surface plasmon (SP) [18]. Geometry of the metal dielectric interface as well as the permittivities of the metal and the surrounding dielectric govern the nature of these electron oscillations in general. Basically, there are 2 types of Surface Plasmons, namely, Localized Surface Plasmons (LSP) and Surface Plasmon Polaritons (SPP) [32]. LSPs are analogous to standing waves which are confined to a certain geometry [33]. They do not propagate in space since the geometry constrains the propagation. SPPs are not confined to a space and they can propagate.

Therefore, the two main types of SPs serve different purposes in plasmonic devices. SPPs are used as signal carriers due to their nature of propagating along

wave guide based signal paths. Since SPPs are non-radiative, specific methodologies such as grating and coupling to a prism are adopted [34]. On the other hand, LSPs can be excited by direct illumination of light. The incident electric field of light generates oscillations that can be sustained through continuous supply of light. For a given geometry, there is a certain frequency of the incident wave which generates a maximum electric field which causes the creation of a maximum number of LSPs. This phenomena is called Surface Plasmon Resonance (SPR) [35]. Throughout this research, we are focusing on LSPs. Therefore, unless otherwise specified, SP means LSP throughout this thesis, from here on.

To understand the properties of SPs on materials, several mathematical models have been proposed. Rigorous analysis as well as back-of –the-envelope type analysis can be done using such models on how the electrons in a metal interact with an external electromagnetic field [36,37]. One of the most established simple models is the Jellium model [10, 38] in which free electrons are modelled to behave as a gas and roam around a uniform, fixed distribution of positive charges, ensuring electrical neutrality of the system.

In contrast, photons cannot be confined to a space less than the diffraction limit, which is usually in the sub wave length scale [39, 40]. One of the major advantages of SPs is their ability to be confined into length scales less than the sub wave length dimensions, which are below 300 nm [34]. Therefore, to fabricate optical devices in the nanoscale, manipulation of SPs is required instead of photons [8].

2.1.2 Stimulated Emission

Absorption and spontaneous emission are two of the well-known energy transferring processes that take place in atoms [41–43]. Electrons are placed in discrete energy levels in atoms. When the energy difference between two energy levels

equals the energy of the incident photon, that energy is absorbed by an electron to transfer from the lower energy level to the upper energy level. This process is called absorption. Similarly, an electron in an upper/excited energy level can relax to come down to a lower level which is known as spontaneous emission. In addition, there is another process called "stimulated emission" which was predicted by Einstein [44]. He postulated that the presence of a photon can cause an electron to relax down to a lower level. Simply, an excited electron in a higher energy level can drop down to a lower level while emitting another photon which is identical to the incoming photon which stimulated the process. For this to happen, the number of photons in the upper level should be larger than the number of photons in the lower level, which means that there should be a positive population inversion. This prediction led to the discovery of coherent amplification of light. Consequently, this triggered the invention of lasers [45, 46].

The acronym laser stands for light amplification by stimulated emission of radiation. Studying how the laser works gives a lot of insights to study about the spaser since there are lots of similarities in structure and operation. In a laser there are excitable atoms which act as a gain medium. The atoms are excited by pumping energy externally, which is usually incoherent. There is an optical cavity as well which provides feedback for the lasing operation to sustain. When the external pump continuously supplies energy, electrons in the gain medium get excited. Some of the excited electrons start to decay by spontaneous emission. As the external pump continues to provide energy, atoms achieve population inversion gradually. This causes stimulated emission to occur, through the effect of photons that have already been generated via spontaneous emission. The number of emitted coherent photons is multiplied which implies that the output is amplified as a coherent light beam [46]. Stimulated emission of photons is now a well-established phenomenon with lots of commercial applications as well [47].

Stimulated emission of surface plasmons

Bergman and Stockman predicted the possibility of stimulated emission of SPs in 2003 [19]. Photons are bosonic with a spin 1 intrinsic angular momentum and they are electrically neutral, while SPs also possess the same properties [48]. That generally prompted both Stockman and Bergman to form such a claim on stimulated emission of SPs. This was experimentally proven by Seidel *et al.* in 2005 [49].

2.1.3   Spaser

The acronym spaser stands for surface plasmon amplification by stimulated emission of radiation. Similar to the generation of coherent light by stimulated emission of photons in lasers, a spaser is designed as a coherent SP source which operates through stimulated emission [11]. The structural components are analogous to those of the laser since a spaser is the nano-scale counterpart of laser. So there are two main components in a spaser in general, namely the plasmonic resonator and the gain medium. The plasmonic resonator, similar to the laser cavity, supports SP modes. The gain medium is comprised of quantum emitters (i.e. chromophores) and it provides amplification to the SPs to sustain the oscillations.

Some of the widely used plasmonic gain mediums are quantum wells [50], quantum dots [51], dye molecules [52, 53] and carbon nano-tubes [54, 55]. On the other hand, nano-particles of noble metals [56–58], Aluminium [59], graphene [60], Molybdenum Disulfide [61] and Plasmene [62] are widely used as plasmonic resonators.

The gain medium gets excited continuously when it receives sufficient energy. Therefore, the electrons can absorb the incident energy and travel to excited states. When population inversion takes place, these electrons are stimulated by resonant SP modes of the resonator to relax and transfer energy back into the same SP mode non-radiatively. This process is a feedback which is analogous to
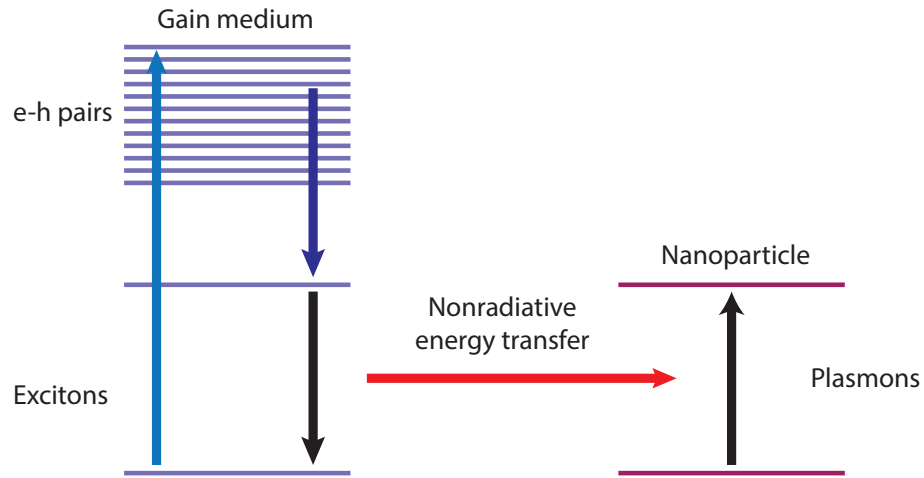
Figure 2.1: Basic operation of a spaser: gain medium excites SP modes in the resonator by stimulated emission of SPs.

the cavity in a laser. This feedback mechanism enhances the number of SPs in a given mode and it creates highly concentrated electric fields within a confined volume, usually in the range of nanometers [11, 19, 30]. This is smaller than the confinement that can be achieved by conventional photonic lasers. The energy flow diagram of a spaser is shown in Fig. 2.1

As indicated in Fig. 2.1, as a result of the energy provided to the gain medium chromophore via pumping, the state of an electron goes to its higher state (blue arrow) and relaxes down to a transitional state (dark blue arrow). The resulting state of the gain medium is called an exiton. These exitons are stimulated by the SPs and release energy to come back to its original ground state (black arrow). The energy is transmitted non-radiatively to the SP mode as explained earlier, creating a feedback mechanism.

Spasers can be designed in different configurations and can be categorized accordingly. One way of classifying is the dimensionality of confinement, one-dimensional [63], two-dimensional [25] and three-dimensional [64]. Spasers can be further divided into two categories as optically pumped [55] and electrically pumped spasers [65].

Properties of Plasmonic Resonators

Designing and fabricating a nano-scale laser with photons is impossible since the size of the laser cavity is restricted by the diffraction limit which is half a wavelength of the electromagnetic wave we intend to make use of [66]. The wavelength of light is higher than 300nm and it is expected to reduce device dimensions below 100nm to achieve nano-scale miniaturization [34]. On the contrary, the diffraction limit does not restrict the surface plasmons (LSPs or simply SPs) from confining the electromagnetic energy at nano-scale dimensions [67]. Consequently, it is possible to generate intense, coherent and localized plasmonic fields in nano-meter range using a plasmonic resonator.

The size of the resonator is limited only by its non-locality radius $l_{nl} = V_F/\omega$, where V_F is the Fermi velocity of electrons in the metal and ω is the plasmon frequency [68]. Non locality radius is usually in the range of 1 nm for noble metals such as Silver and Gold, which gives far better miniaturization and confinement than the photonic resonators [69].

2.1.4   Permittivity models of materials

In order to calculate the response of a free-electron gas on a bulk material subject to a time varying electric field, a proper estimate of the permittivities of the plasmonic material as well as the surrounding dielectric is essential.

Johnson and Christy has experimentally calculated the permittivity values of many bulk materials such as silver and gold [70]. Another widely accepted model is the Drude model given by the following formula.

$$\epsilon_{\text{Drude}}(\omega) = \epsilon_0 - \frac{\epsilon_0 \omega_p^2}{\omega^2 + i\gamma(\omega)\omega}, \qquad (2.1)$$

where $\gamma(\omega)$ is the characteristic collision frequency [34]. This formula is valid if the smallest dimension of the bulk material is larger than the elastic mean-

free path l_{ef}. The corrections for the non-locality effects have been proposed in [71]. Since we are mostly studying about the geometries whose smallest dimensions are larger than the non-locality radius, we will use the Drude model or the Johnson-Christy model accordingly, and the model will be clearly mentioned where relevant.

Furthermore, the following requirement should also be satisfied for the existence of plasmons in a nanoparticle (2.1)

$$Re(\epsilon_m) < 0, \tag{2.2}$$

$$Im(\epsilon_m) \ll -Re(\epsilon_m), \tag{2.3}$$

where ϵ_m is the permittivity of the nanoparticle [18].

2.2 Theoretical Work

Since year 2003, there has been substantial progress in the research on spasers. Interactions between the active medium and the plasmonic resonator, various resonator geometries and materials have been theoretically studied [10,18]. There has been a few practical realizations as well [30].

2.2.1 Spectral Representation

The ability to estimate the plasmon resonance modes of nanoparticles is essential for both analysis and design of spasers. The excitable plasmon resonance modes are decided by several factors such as the particle size, shape, material composition, and surrounding environment [72]. In 2003, Bergman and Stockman used the method called Spectral Representation to explain the operation of a spaser [10] [18]. Separation of geometrical contributions from those of the di-

electric and metal properties when describing the plasmonic resonances is the special property of the spectral representation method, which is really crucial in obtaining a thorough understanding about spasers. Spectral representation formalism provides the ability to separately study the material response and geometric effects and it provides a convenient framework in the design process as well. Therefore, spectral representation method has been adopted by many in literature to describe the spaser phenomena [10].

The SP Eigen modes $\psi_n(r)$ are described by a wave equation

$$\nabla[\Theta(r)\nabla_n(r)] = s_n\nabla^2\psi_n(r), \tag{2.4}$$

where s_n is a real Eigen value ($0 \leq s_n \leq 1$) corresponding to a plasmon mode n [11,18]. $\Theta(r)$ is the characteristic function which is equal to 1 for metal and 0 for dielectric. Moreover, the SP mode frequency ω_n satisfies $\Re(s(\omega_n)) = s_n$, where $s_{(\omega)} = \epsilon_d/(\epsilon_d - \epsilon_m(\omega))$ is the Bergmans' spectral index.

2.2.2   Proposed spaser Geometries

One of the first structures proposed for spasers was a V-shaped metallic nanoparticle coupled to a semiconductor quantum dot (QD) gain medium [19]. Another significant contribution was made in terms of the geometry of the plasmonic resonator when a metallic bowtie structure was introduced in [23]. Some of the other relevant nanoparticle shapes studied for their plasmonic modes include spheres [19], truncated spheres [73], hemispheroids [74], nano-shells [75], cubes [76], tetrahedra [77], nano-rods [78] and disks [79].

Out of the many types of quantum emitters (chromophores), quantum dots (QDs) have been utilized as the gain medium in most of the spasing configurations, since they have a better thermal stability. There are instances where other types of gain mediums such as quantum wells and rare earth ions have been

used [3]. Furthermore, QDs have an atomistic behavior with a well-defined spectral response [80].

2.2.3 Modelling spasers

In order to understand the physics of spasers, several analytical models have been developed. Most of them model the problem in a quasi-classical approach [11,31] whereas fully quantum models have also been developed [81].

Stockman *et al.* have quantum mechanically analyzed the interaction between a metal nanoparticle and closely located gain elements, which are modeled as two level systems (TLS), where a pump source is present to continuously excite them [11,19]. Pumping excites electrons in the ground state to absorb energy and elevate to levels which are above the 2nd energy level. One major assumption in modelling the gain medium as TLS is that the decay rate from the higher levels to the 2nd level is very high so that we do not have any control over such transitions. That provides a lot of simplification to the spaser equations as well [18]. Dorfman *et al.* in [31] have considered an additional 3rd level in the gain medium to achieve more control over the output.

The Hamiltonian of the system has been derived by treating the Surface Plasmon-Gain medium interactions quantum mechanically while the interactions between the pump photons and the gain mediums have been modelled quasi-classically [11]. The Liouville-von Neumann master equation is written by either assuming a closed system with no interactions with the environment, or else it has been modified with suitable Markovian super-operators to derive a set of density matrix equations to solve the system [11,19,82]. Performance parameters such as threshold pump power, plasmon statistics, spasing frequency, plasmon decay rates and plasmon Q-factor have been studied extensively for TLS [11].

Apart from the conventional materials such as Silver and Gold, new materials

such as Graphene and Molebdinum Disulphide have been used to model spasers recently [55, 83].

2.3   Experimental Realizations and Applications

Seidel *et al.* proved the concept of stimulated emission of SPs in practice by amplifying the SPs at the interface between a flat continuous Silver film and a liquid of organic dye molecules [49]. Since then, several experiments have been conducted to fabricate metamaterials that can compensate losses [26].

Noginov *et al.* [30] performed the first demonstration of a spaser in 2009 where they used a gold nano-sphere of radius 7 nm surrounded by dye molecules as gain mediums. The gain mediums were contained in a 15 nm thick silica shell. Optical pumping was used as the external incoherent pumping method. The radius of the whole spaser configuration was 44 nm. Another experimental demonstration of nanometre-scale plasmonic lasers, which generated optical modes a hundred times smaller than the diffraction limit, is reported in [25]. The design is a nanolaser made of a hybrid plasmonic waveguide consisting of a high-gain cadmium sulphide semiconductor nanowire, separated from a silver surface by a 5 nm thick insulating gap. Furthermore, an experimental realization of a three-level spaser was reported in 2018 by Song *et al.* [27], where they have utilized triplet state electrons as the gain medium.

As mentioned earlier as well, a spaser is a nano-scale device which can generate intense and coherent SPs while achieving miniaturization beyond the conventional diffraction limits. As a result, it can be identified as one of most promising cornerstones in nano-electronics. Similar to the way the transistor and the PN junction are identified as the basic devices in semiconductor electronics, spaser may be identified as one of the basic building blocks of ultra-fast and miniaturized opto-electronics in the nano-scale. There are plenty of potential applications

for which the spaser can be made use of.

2.3.1   Prospects in nano-medicine

Nano-medicine is broadly the use of nanotechnology for the enhancement of medicine. It holds an enormous potential towards improving various diagnostic techniques treatment methods [84, 85]. Currently, drug delivery [86], active implants [87] and cancer therapy [88] are some of the hot topics in the rapidly evolving domain of knowledge. Due to their ability to confine optical energy to unprecedented volumes, spasers have been predicted to have good potential to serve as active implants and drug delivery agents in cancer therapy and medical imaging [89].

Due to the undesired side effects such as the destruction of healthy tissues when treating to cancer patients using conventional methods such as chemotherapy and radiotherapy [90], target tumor destruction methodologies have emerged [91]. The development of such an effective technique to treat cancer is one of the major frontiers that medical research.

Since the spaser can generate tightly confined, intense electric fields, it has been proposed for cancer therapy [55]. However, due to the inefficiency of output generation, higher threshold values and less controllability, spaser technology should be improved to suit the needs of nano-medicine. In our presented in this thesis, we have come up with a much improved spaser model with high efficiency, lower thresholds and improved controllability, which can enhance the use of spasers in medical applications.

2.3.2   Quantum Computing

The field of quantum computing has received a lot of attention within the scientific community, for the incomparable processing speeds it promises [92]. The

basic computational element of a quantum computing is called a qubit, analogous to a bit in conventional computing. Qubits can take more than two states compared to a bit which takes only '0' and '1'. A qubit can be in superposition of '0' and '1'. Therefore, a quantum system with observable quantities using eigenvalues is a contender to implement a qubit. Therefore, there is a significant potential for the spaser to be a part of a system which produces qubits. On the other hand, a future quantum computer may requires nano-optical sources, amplifiers, modulators and switches since optical devices can operate faster than the conventional electronic devices. Therefore, it is highly likely that spasers may be used in super computers. The potential of their use has been enhanced through the improved characteristics, design capabilities and physical insights generated through our work, presented in this thesis.

2.3.3   Optical-lithography

Optical lithography is a major branch in nano-lithography, which refers to the main nano-scale fabrication techniques [93]. Specifically, optical lithography makes use of very short light wavelengths to change the solubility of certain molecules, which etches raw nano-materials to form desired structures. Due to the limit of diffraction, there is a lower limit to the wavelengths that can be generated by lasers. To achieve much smaller feature dimensions in nano-structures, spasers can replace lasers in optical lithography. The proposed spaser and the analysis we conduct in this thesis can enhance the possibility of using the spasers in these nano-fabrication techniques, whilst providing improved controllability.

2.3.4   Nano-scopy

Nano-scopy broadly refers to the techniques that have emerged to exceed the boundaries of microscopy, by going below the optical limits of 200-300 nm imag-

ing [94]. Spaser can become a key device in achieving diffraction unlimited imaging methods [95]. The necessity of a device which can confine optical energy going beyond the limits of diffraction can be achieved through the manipulation of the proposed spaser models in this thesis.

The new knowledge presented in this thesis will enrich the domain of active nano-plasmonics and will significantly enhance the potential of spasers in many different applications.

This page intentionally left blank.

Chapter 3

Analytical characterization of the spasing curve

In this chapter, we derive approximate analytical expressions to characterize the spasing (L-L) curve of a coherently enhanced spaser with 3-level gain-medium chromophores. It enables optimization of the large parameter space associated with spaser designing, a functionality not offered by the methods currently available in literature.

Due to the compact nature of the analytical expressions derived in this chapter, grouping and identification of key processes responsible for spasing action can also be analysed. Significant physical insights have been derived as well. Furthermore, we show that our expression generates results within 0.1% error compared to numerically obtained results for pumping rates higher than the spasing threshold, thereby drastically reducing the computational cost associated with spaser designing. All these results would be vital for advancing the spaser technology towards the level of device realization.

3.1 Introduction

Developing efficient, reliable and easily controllable spasers is one of the major research areas in nano-plasmonics. Researchers have identified several performance parameters to be given attention for improvement. Some of such key pa-

rameters are number of surface plasmons per spasing mode (which represents the power output), spasing threshold and spasing frequency. All spaser models that have been proposed have low output efficiency, generating a few plasmons per spasing mode [11, 19]. Secondly, many of the proposed designs have very high spasing thresholds, which naturally discourages the utility of spasers in many of the potential applications [96]. On the other hand, most spasers that have been designed in literature have fixed spasing frequencies which are decided by the inherent properties of the plasmonic resonator and the gain medium [10, 18]. The ability to control the spasing frequency from outside is much desirable to expand the potential applications of spasers.

In most of the research that have been done on spasers, the gain medium has been modelled as a Two Level System (TLS) which has only one mode of external input, which is usually through incoherent pumping [26, 97, 98]. Apart from the analytical simplifications that it brings in for the analysis of spaser dynamics, many drawbacks have been identified in terms of spaser performance [82, 96]. Many of these effects arise due to the gain saturation caused by the plasmonic feedback on the gain medium chromophores. Increasing the pumping power as a solution is not desirable since it increases the ohmic losses due to heating [31]. A bi-stable spaser has been proposed [11] which is also not feasible in terms of fabrication.

3.2   Three-level model

Dorfman *et al.* [31] has proposed a new scheme which models the gain medium chromophores as 3-level systems. One of the main assumptions in a TLS is that the decay rate of the excited electrons from a higher level to the second energy eigen state is infinite [11]. That assumption is released in the proposed model, and the electron transitions between level 3 and level 2 are controlled by a new

coherent electric field. The introduction of such a control is expected to enhance the number of SPs per spasing mode while reducing the spasing threshold by an order of magnitude. Dorfman has numerically shown that this claim is valid for several cases. However, the model needs an extensive simulation for validation, due to its potential. Moreover, the operating principles and characteristics of the device should be further analysed to build a complete model for potential applications.

Since the new scheme is predicted to enhance the plasmon statistics immensely, a further analytical characterization of the numerical results will benefit future research based on the 3-level gain mediums. In this chapter, we have derived expressions analytically to describe the number of SPs per spasing mode, which is the physical property that indicates the power output of the device. All the system properties such as decay rates, number of gain medium chromophores, material and geometry of the resonator as well as the energy losses to the environment have been incorporated in these derivations. The behavior of the output power of the spaser is what is referred to as the spasing curve [11], which is analogous to the L-I (Light output (L) vs current (I)) curves in semi-conductor lasers [99, 100].

3.3 The spasing process

The basic configuration and the energy flow diagram of our system are illustrated in Fig. 3.1. A plasmonic nano-structure is surrounded by an optical gain medium which comprises homogeneously distributed generic 3-level quantum emitters such as semiconductor quantum dots [101–103], rare earth ions or atoms [104, 105]. We have used the Bra-Ket notation throughout the analysis. An emitter has a ground state ($|1\rangle$), as well as two excited states, ($|2\rangle$ and $|3\rangle$). The two inputs to the spaser are denoted by the incoherent pumping rate g (coupled to the tran-

sition $|1\rangle \rightarrow |3\rangle$) and the Rabi Frequency of the coherent input field Ω_a (coupled to the transition $|2\rangle \rightarrow |3\rangle$). Since we are interested in the continuous wave (CW) operation of the spaser, g and Ω_a will be provided continuously as long as the spaser works, in order to sustain the SPs. The spasing transition $|2\rangle \rightarrow |1\rangle$ represented by the corresponding Rabi frequency Ω_b, is coupled with a surface plasmon mode in the nano-plasmonic resonator to transfer energy non-radiatively from the chromophores to the SPs, thereby sustaining the spasing process. The plasmonic field generated in the nano-structure provides an internal feedback to the gain medium during operation. The spontaneous decay rates in the 3-level emitters are denoted by γ_{21}, γ_{32} and γ_{31}, as indicated in Fig. 3.1. The total number of 3-level quantum emitters (chromophores) in the gain medium is denoted by N_c.

3.4   The formalism

To simplify our analysis, we approximate the 3-level emitters as dipoles [10]. Rotating Wave Approximation (RWA) has been deployed to neglect the rapidly oscillating terms in the Hamiltonian [18]. Then, the total Hamiltonian of the gain medium in the interaction picture can be written as

$$H_{int} = \Sigma_p \begin{pmatrix} -\hbar\Delta_b^{(p)} & \hbar\Omega_b^{*(p)} & 0 \\ -\hbar\Omega_b^{(p)} & 0 & -\hbar\Omega_a^{*(p)} \\ 0 & -\hbar\Omega_a^{(p)} & \hbar\Delta_a^{(p)} \end{pmatrix} \tag{3.1}$$

It can be expressed in Dirac notation for the ease of expression, as follows:

$$\begin{aligned} \mathcal{H}_{int} = \Sigma_p \{ &-\hbar\Delta_b^{(p)} |1\rangle \langle 1| + \hbar\Delta_a^{(p)} |3\rangle \langle 3| \\ &- (\hbar\Omega_b^{(p)} |2\rangle \langle 1| + \hbar\Omega_a^{(p)} |3\rangle \langle 2| + c.c) \}, \end{aligned} \tag{3.2}$$
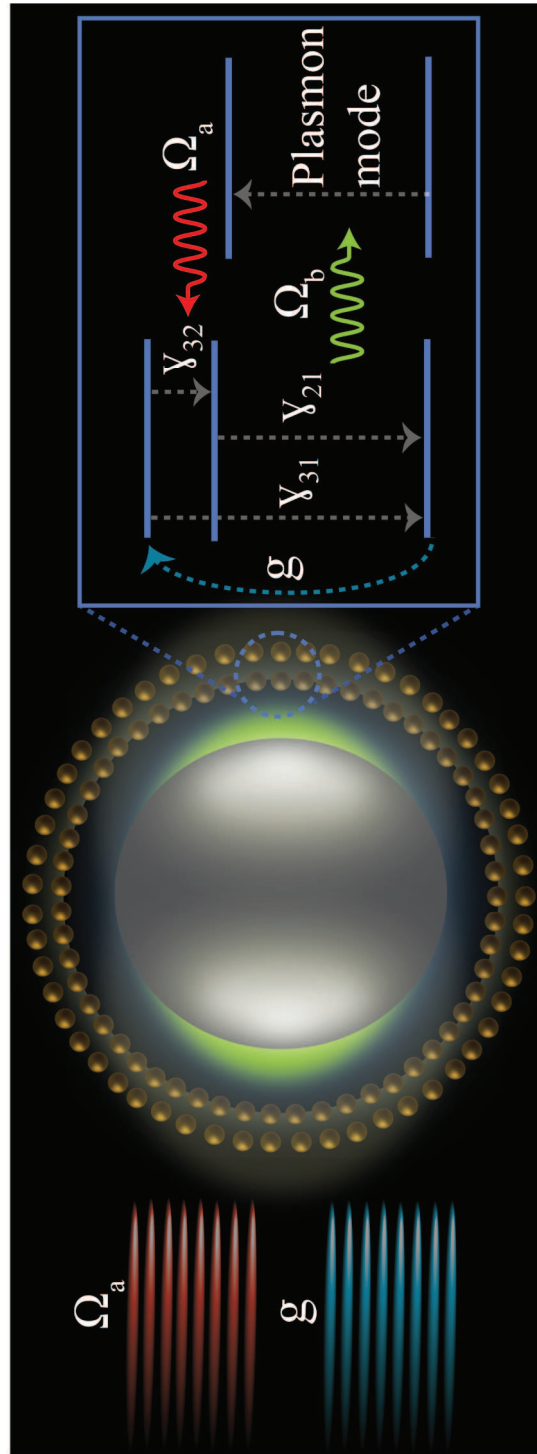
Figure 3.1: The basic structure and the energy flow diagram of a 3-level spaser

where *c.c.* denotes the complex conjugate and $\hbar$ is the reduced Plank's constant. The Hamiltonian takes into account the summation of all the N_c chromophores (quantum emitters) and that is denoted by Σ_p. We assume that the inter chromophore interactions are comparatively weak enough to be neglected when writing the Hamiltonian [10, 11, 18]. In Eq. (3.2), detunings are defined as $\Delta_a = \omega_{32} - \omega_a$ and $\Delta_b = \omega_{21} - \omega_b$ [106], where ω_{32} and ω_{21} are the frequencies of the corresponding band gaps of the chromophores and ω_a and ω_b are defined as the frequencies of the coherent field and plasmonic field respectively.

Standard semiclassical theory has been adopted in the analysis, where the gain medium is treated quantum mechanically and the SPs as well as photons are treated as classical quantities [11, 31]. Therefore, we express both plasmon annihilation operator, $\hat{a}_n$, and the photon annihilation operator, $\hat{b}_m$, as time varying complex numbers (C-numbers) with definitions $a_n = a_{0_n} e^{-i\omega_s t}$ and $b_m = b_{0_m} e^{-i\omega_{32} t}$ [10]. a_{0_n} and b_{0_m} are slowly varying amplitudes whereas ω_s is the frequency related to spasing.

Based on the above information, the number of SPs per n^{th} spasing mode [18] can be expressed as

$$N_n = |a_{0_n}|^2. \tag{3.3}$$

$\Omega_b^{(p)}$ is expressed as $-A_n d_{21}^{(p)} \nabla \psi_n a_{0_n} / \hbar$ where

$$A_n = \left(\{ 4\pi\hbar \, \mathrm{Re}[s(\omega_n)] \} / \{ \epsilon_d \, \mathrm{Re}[ds(\omega_n)/d\omega_n] \} \right)^{1/2} \tag{3.4}$$

Here, $s(\omega_n) = \epsilon_d / [\epsilon_d - \epsilon_m(\omega_n)]$ where ϵ_d is the bath permittivity and $\epsilon_m(\omega_n)$ is the permittivity of the metal at plasmon resonance frequency ω_n. Dipole moment element of the gain chromophores is given by d_{21} and the gradient of the potential function $\nabla \psi_n \approx 1/\sqrt{V}$ where V is the modal volume of the electric field generated by the plasmon mode, which is directly related to the size and shape of the nano-particle [31, 107].

Furthermore, Ω_a is considered a constant since we assume that the driving field is strong enough to maintain the number of photons in mode m constant under operating conditions [31].

3.5   Density Matrix Equations

The pth 3-level gain medium chromophore is modelled as an open quantum system using the Liouville-von Neumann master equation,

$$\dot{\rho}^{(p)} = -i/\hbar[\mathcal{H}_{int}, \rho^{(p)}] - \mathcal{L}\rho^{(p)}, \tag{3.5}$$

where $\dot{\rho}^{(p)}$ represents the time derivative of the density matrix. $\mathcal{L}$ is the Lindblad super-operator that quantifies the interactions with the environment such as, spontaneous decay of the gain medium, incoherent pumping and dephasing (decoherence) [108]. Lindbladian terms have been extracted from [31, 81, 109]. The off diagonal relaxation rates are

$$\Gamma_{21} = \frac{1}{2}(\gamma_{21} + g) + \gamma_{ph} + i\Delta_b, \tag{3.6}$$

$$\Gamma_{31} = \frac{1}{2}(\gamma_{31} + \gamma_{32} + g) + \gamma_{ph} + i(\Delta_a + \Delta_b), \tag{3.7}$$

$$\Gamma_{32} = \frac{1}{2}(\gamma_{31} + \gamma_{32} + \gamma_{21}) + \gamma_{ph} + i\Delta_a, \tag{3.8}$$

where γ_{ph} is the dephasing (decoherence) rate of ρ_{ij} [31]. Hence, the emitter density matrix elements ρ_{ij} are given by the following complex valued coupled partial differential equations.

$$\dot{\rho_{11}} = \gamma_{21}\rho_{22} + \gamma_{31}\rho_{33} - g\rho_{11} + i(\Omega_b^*\rho_{21} - \Omega_b\rho_{21}^*), \tag{3.9}$$

$$\dot{\rho_{33}} = -(\gamma_{31} + \gamma_{32})\rho_{33} + g\rho_{11} - i(\Omega_a^*\rho_{32} - \Omega_a\rho_{32}^*), \tag{3.10}$$

$$\dot{\rho_{21}} = -\Gamma_{21}\rho_{21} - i\Omega_b(\rho_{22} - \rho_{11}) + i\Omega_a^*\rho_{31}, \tag{3.11}$$

$$\dot{\rho_{31}} = -\Gamma_{31}\rho_{31} - i\Omega_b\rho_{32} + i\Omega_a\rho_{21}, \tag{3.12}$$

$$\dot{\rho_{32}} = -\Gamma_{32}\rho_{32} - i\Omega_a(\rho_{33} - \rho_{22}) - i\Omega_b^*\rho_{31}, \tag{3.13}$$

$$\rho_{11} + \rho_{22} + \rho_{33} = 1, \tag{3.14}$$

We describe the stimulated emission of SPs as their excitation by the coherent polarization of the gain medium corresponding to the transition $|2\rangle \rightarrow |1\rangle$. Therefore, the time evolution of the plasmon annihilation operator should be of the same form as that of a 2-level gain medium [10], which is expressed by invoking the Heisenberg equation of motion for a_{0_n} as

$$\dot{a_{0_n}} = -\Gamma_n a_{0_n} + i\Sigma_p \rho_{21}^{(p)}\tilde{\Omega}_b^{(p).} \tag{3.15}$$

SP relaxation rate Γ_n is expressed as $\gamma_n + i\Delta_n$ where γ_n is the plasmon decay rate, and Δ_n is the detuning between ω_n and the frequency of the $|2\rangle \rightarrow |1\rangle$ transition (ω_{21}). γ_n generally depends on the optical frequency, permittivities and system geometry [18].

The value $\tilde{\Omega}_b^{(p)}$ is the single plasmon Rabi frequency denoted by $\tilde{\Omega}_b^{(p)} = \Omega_b^{(p)}/a_{0_n}$. Next we assume that all N_c chromophores interact with the SPs identically, hence we omit the index p and set $\Sigma_p \rightarrow N_c$ in Eq. (3.15). Next, by writing the complex variables and coefficients in Eq. (3.9 - 3.14) and Eq. (3.15) in the form of $z = \text{Re}(z) + i\text{Im}(z)$ and by equating the real parts and imaginary parts of the equations separately, we derive a set of real valued, non-linear, coupled differential equations (3.16a-3.16k). Note the labeling we have followed: $\text{Re}(\rho_{cd}) = \rho_{cd}^R$, $\text{Im}(\rho_{cd}) = \rho_{cd}^I$, $\text{Re}(a_{0_n}) = \mathcal{A}$ and $\text{Im}(a_{0_n}) = \mathcal{B}$. Furthermore, Δ_a and Δ_b are taken as zero since resonant coupling is assumed between relevant interactions. Hence,

all Γ_{cd}s are assumed real [10, 31].

$$\dot{\rho}_{11} = \gamma_{21}\rho_{22} + \gamma_{31}\rho_{33} - g\rho_{11} + 2\tilde{\Omega}_b(B\rho_{21}^R - A\rho_{21}^I) \tag{3.16a}$$

$$\dot{\rho}_{33} = -(\gamma_{31} + \gamma_{32})\rho_{33} + g\rho_{11} + 2\Omega_a\rho_{32}^I \tag{3.16b}$$

$$\dot{\rho}_{21}^R = -\Gamma_{21}\rho_{21}^R + \tilde{\Omega}_b B\rho_{22} - \tilde{\Omega}_b B\rho_{11} - \Omega_a\rho_{31}^I \tag{3.16c}$$

$$\dot{\rho}_{21}^I = -\Gamma_{21}\rho_{21}^I - \tilde{\Omega}_b A\rho_{22} + \tilde{\Omega}_b A\rho_{11} - \Omega_a\rho_{31}^R \tag{3.16d}$$

$$\dot{\rho}_{31}^R = -\Gamma_{31}\rho_{31}^R + \tilde{\Omega}_b A\rho_{32}^I + \tilde{\Omega}_b B\rho_{32}^R - \Omega_a\rho_{21}^I \tag{3.16e}$$

$$\dot{\rho}_{31}^I = -\Gamma_{31}\rho_{31}^I - \tilde{\Omega}_b A\rho_{32}^R + \tilde{\Omega}_b B\rho_{32}^I + \Omega_a\rho_{21}^R \tag{3.16f}$$

$$\dot{\rho}_{32}^R = -\Gamma_{32}\rho_{32}^R + \tilde{\Omega}_b A\rho_{31}^I - \tilde{\Omega}_b B\rho_{31}^R \tag{3.16g}$$

$$\dot{\rho}_{32}^I = \Omega_a(\rho_{22} - \rho_{33}) - \Gamma_{32}\rho_{32}^I - \tilde{\Omega}_b(A\rho_{31}^R - B\rho_{31}^I) \tag{3.16h}$$

$$\rho_{11} = 1 - \rho_{22} - \rho_{33} \tag{3.16i}$$

$$\dot{\mathcal{A}} = -\gamma_n\mathcal{A} + \Delta_n\mathcal{B} - N_c\tilde{\Omega}_b\rho_{21}^I \tag{3.16j}$$

$$\dot{\mathcal{B}} = -\gamma_n\mathcal{B} - \Delta_n\mathcal{A} + N_c\tilde{\Omega}_b\rho_{21}^R. \tag{3.16k}$$

$N_n = |a_{0_n}|^2$ and $|a_{0_n}|^2 = \mathcal{A}^2 + \mathcal{B}^2$. Surface plasmons are modelled using C-numbers corresponding to bosonic number state representation where N_n denotes the expected number of SPs generated in the spasing mode with frequency ω_n [110]. The total energy output of the spaser is then given by $\hbar\omega_n \times N_n$. Hence, N_n gives a measure of the total output energy of the spaser. So our aim is to simultaneously solve equations (3.16a-3.16k) and derive an analytical expression for N_n. Such an expression would not only reduce the computational burden of calculating the output energy ($\propto N_n$) of the spaser [18], but would also provide numerous advantages for design optimization whilst providing valuable physical insights into the operation of the device.

3.6   Numerical Simulations

To study these equations (3.16a-3.16k) in detail and observe the time evolution of ρ_{cd}, $\mathcal{A}$ and $\mathcal{B}$, we carry out some indicative numerical simulations. A silver nano-sphere of radius 40 nm is used as the plasmonic nano-structure. All parameter values are taken from [11,31,70,111], where $\omega_n = 2.5eV$, $\gamma_n = 5.3 \times 10^{14}s^{-1}$. $\Delta_n = 3.2 \times 10^{12}s^{-1}$. $\gamma_{21} = 4 \times 10^{12}s^{-1}$. $\gamma_{32} = 4 \times 10^{11}s^{-1}$. $\gamma_{31} = 4 \times 10^{10}s^{-1}$. $N_c = 6 \times 10^4$ and $\epsilon_d = 2.25$. The bulk permittivity values of silver are obtained from the Johnson and Christy model [70]. We decided to simulate the proposed novel scheme on a metal core shell geometry since the structural and dynamical parameters of such configurations have been thoroughly studied in literature [112].

3.6.1   Results with zero decoherence

Figs. 3.2-3.4 were obtained by solving the system of equations (3.16a-3.16k) for steady state, assuming $\gamma_{ph} = 0$. One of the main objectives of this stage of our research was to study the effect of coherent drive for the performance parameters of the spaser, such as the number of SPs per spasing mode (N_n) and spasing threshold (g_{th}). The results shown in Fig.3.2 shows a significant order-of-magnitude improvement of N_n as Ω_a is increased for higher values of g. Furthermore, the spasing threshold (g_{th}) is also decreased approximately by a factor of 2 for $\Omega_a > 0$. Some of these results have been reported in [31].

It is also observable in Fig.(3.3) that the enhancement of the number of SPs corresponds to a reduction of the population inversion on the spasing transition. The total inversion ($\rho_{33} + \rho_{22} - \rho_{11}$) stays positive, as per Fig.3.4.

All these improvements in N_n and g_{th} are possible due to the quantum coherence that is induced on the 3-level gain medium chromophores by the coherent drive Ω_a.
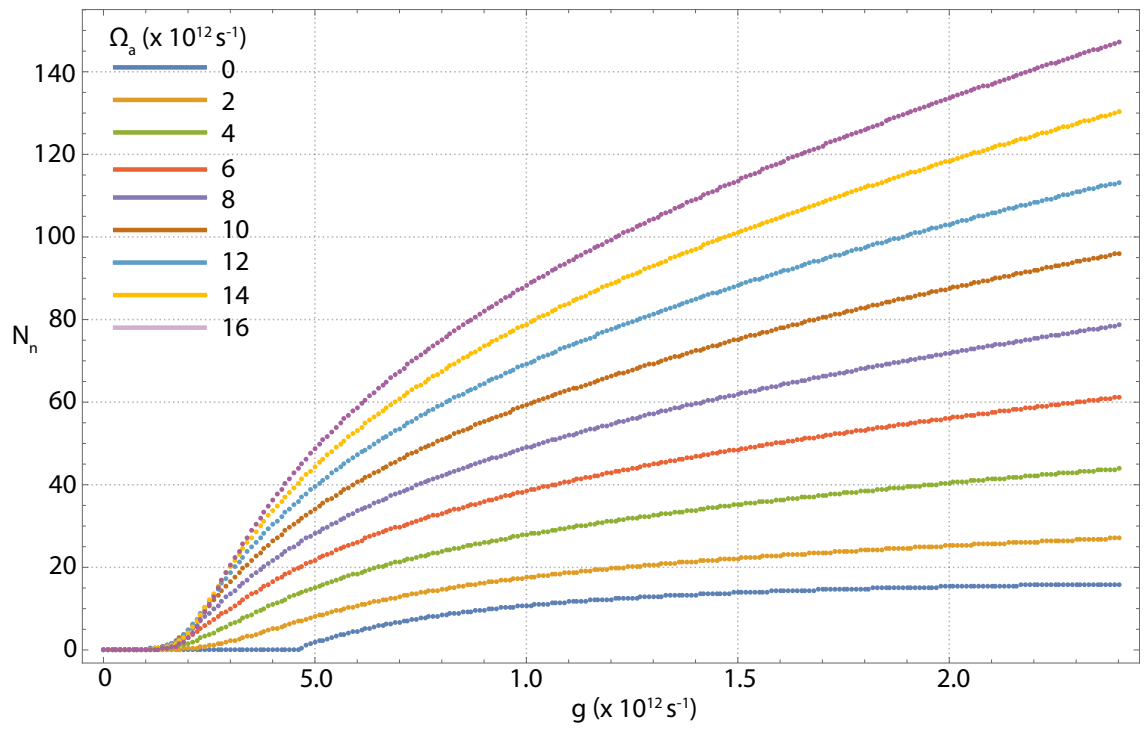
Figure 3.2: Number of Surface Plasmons per spasing mode vs the incoherent pumping rate for different values of Ω_a
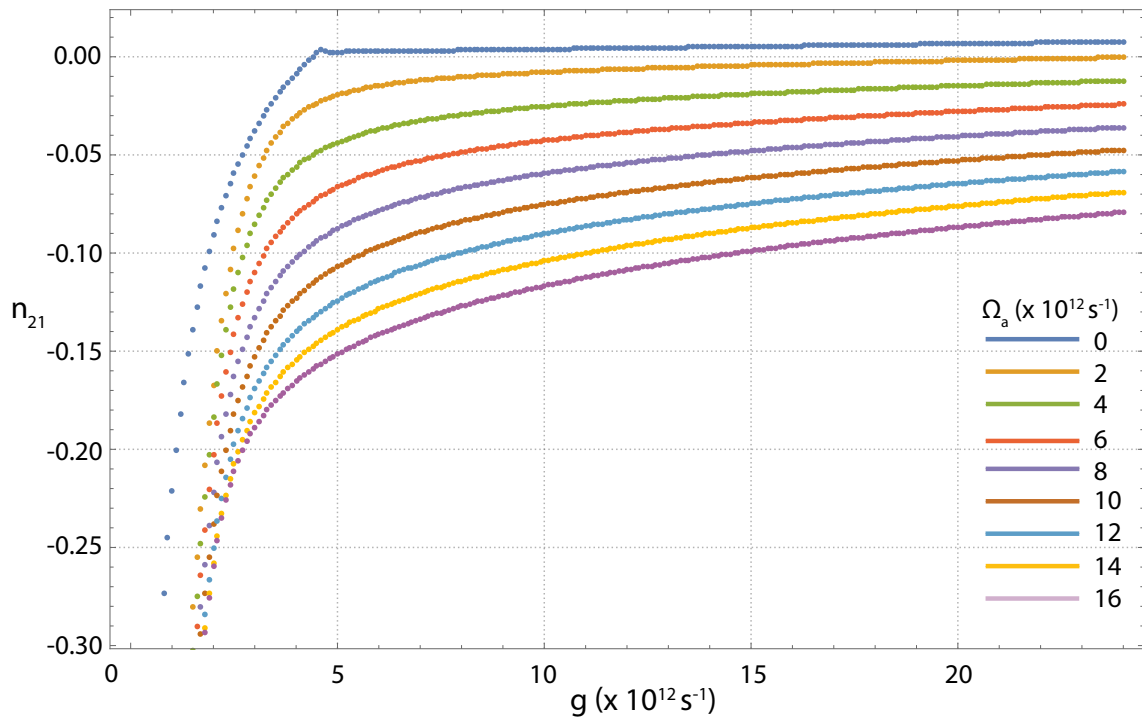
Figure 3.3: The population inversion vs the incoherent pumping rate for different values of Ω_a
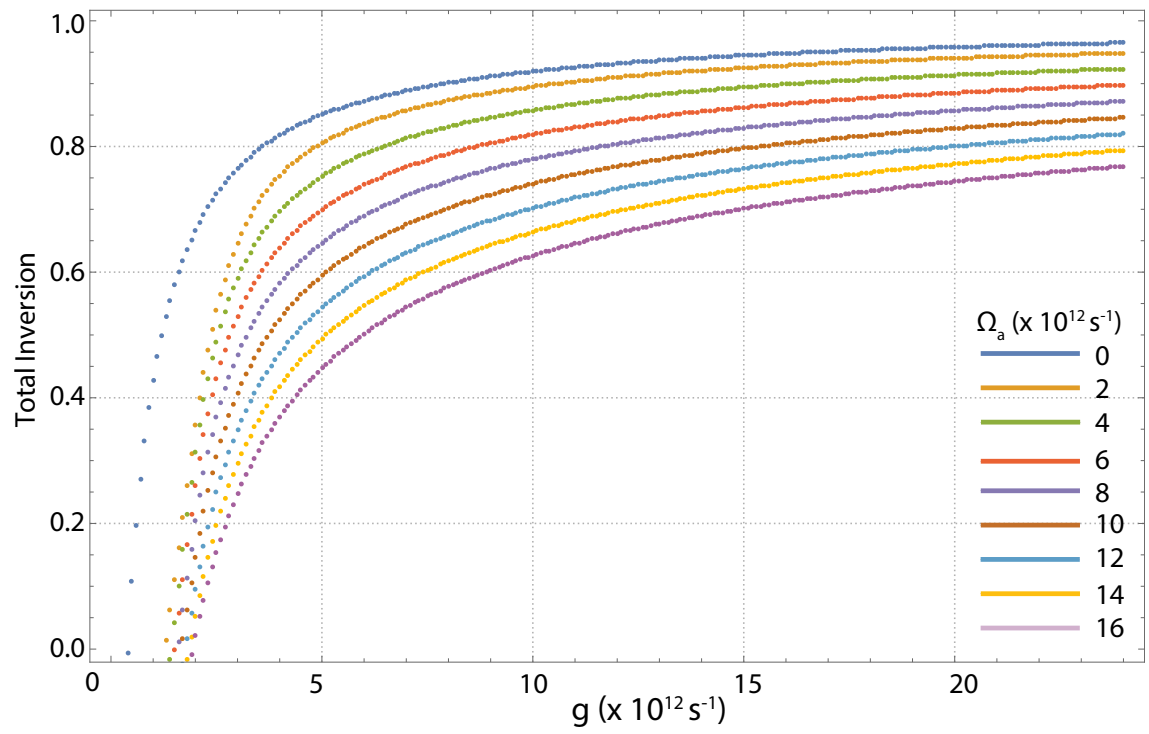
Figure 3.4: The total inversion vs the incoherent pumping rate for different values of Ω_a
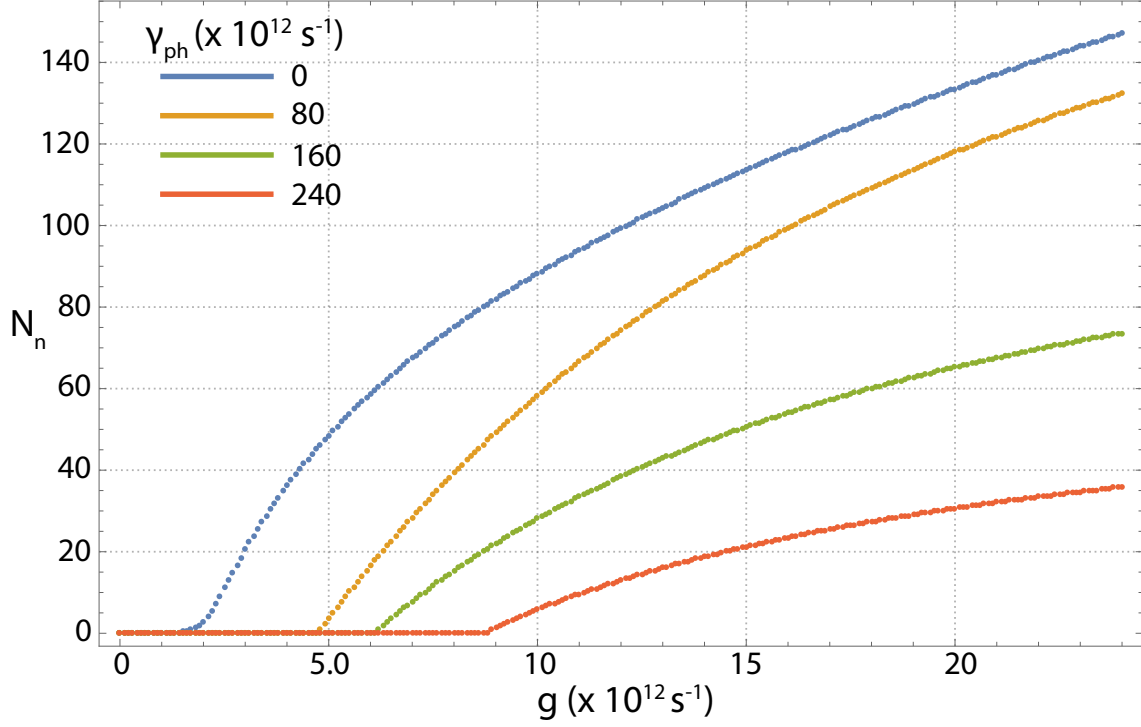
Figure 3.5: Number of SPs N_n versus the incoherent pumping rate g for different decoherence rates $\gamma_{ph} = 0, 80, 160$ and 240×10^{12} for $\Omega_a = 16 \times 10^{12} s^{-1}$

3.6.2 Robustness against decoherence

We conducted a separate set of simulations to study the effects of decoherence ($\gamma_{ph} > 0$) on the spasing statistics. We have demonstrated the effect of decoherence on the number of SPs in fig.3.5 where the number of SPs get reduced for a given value of incoherent pumping rate (g) as the rate of decoherence increased. In fig.3.6, the ability to enhance the number of SPs for a given γ_{ph} by increasing Ω_a is depicted. Therefore, it is evident that by increasing the strength of the coherent drive, it is possible to make the 3-level spaser more robust against decoherence (dephasing) effects.
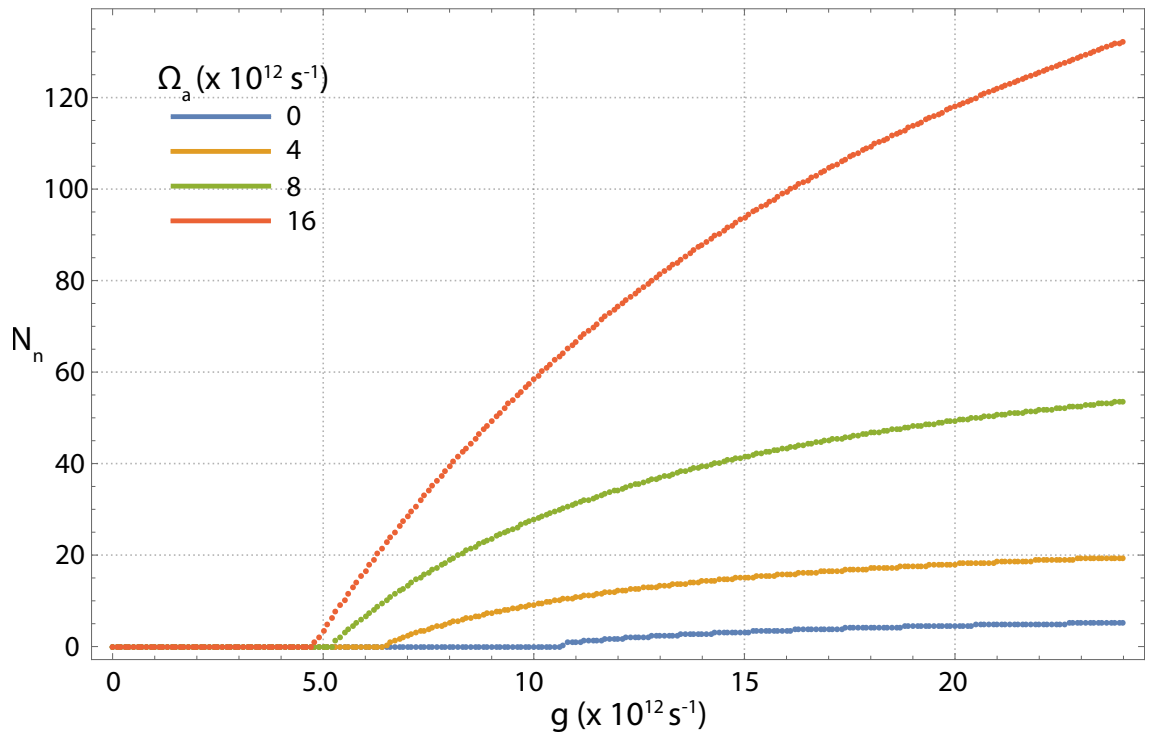
Figure 3.6: Number of SPs N_n versus the incoherent pumping rate g for different strengths of coherent drive $\Omega_a = 0,4,8$ and 16×10^{12} for $\gamma_{ph} = 80 \times 10^{12} s^{-1}$
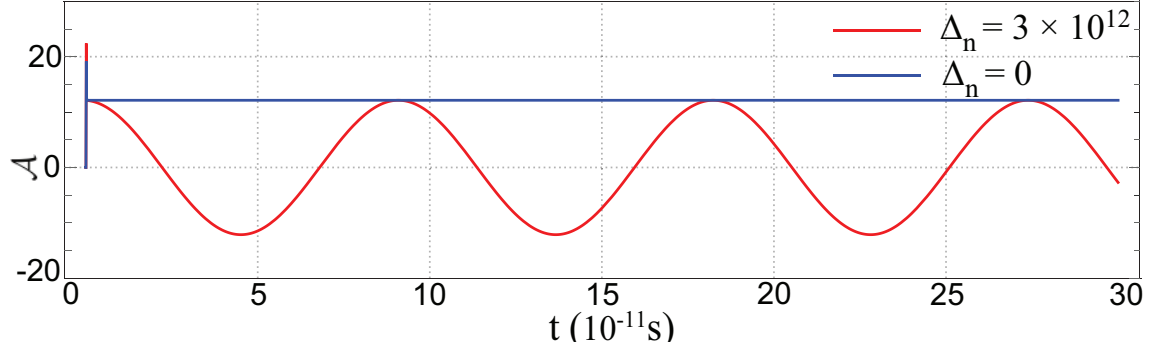
Figure 3.7: Time evolution of $\mathcal{A}$ when $\Delta_n = 0$ and $\Delta_n = 3 \times 10^{12} s^{-1}$. When the spasing transition ($|2\rangle \to |1\rangle$) is resonantly coupled with the SP mode, the complex number representation of the plasmon annihilation operator (a_{0_n}) after the initial transients becomes a constant over time. When there is a significant detuning (i.e. $\Delta_n \neq 0$), a_{0_n} varies sinusoidally over time.

3.7   Analytical Characterization

Numerical results provide an understanding about the improvements that can be made using a coherent drive to control the 3-level gain medium chromophores. In order to develop an in-depth understanding of the variations of SPs with the system parameters and the controlling fields, analytical expressions are required. Not only will it provide an intuitive understanding about the operation of spasers, but will immensely benefit the use of coherent drives and 3-level gain mediums to improve the performance of active nano-plasmonic devices. The time evolution of $\mathcal{A}$ is given in Fig. 3.7 for an incoherent pumping rate (g) of $24 \times 10^{12} s^{-1}$. Due to the inherent slowly varying nature of the C-numbers (a_{0_n} and ρ_{cd}s for $c \neq d$) [11], multiple rounds of detailed numerical simulations show that all time derivatives in Eq. (3.16a-3.16k) do not become zero simultaneously, even at steady state for any g or Ω_a. Since $\Delta_n \ll \gamma_n, \omega_n$, we now assume that the $|2\rangle \to |1\rangle$ transition and the SP mode are resonantly coupled (i.e. $\Delta_n = 0$), and carry out the same set of numerical simulations. Note that such an assumption is physically justifiable as well, since the system designers always strive to achieve near or perfectly resonant coupling. The time evolution of $\mathcal{A}$ when $\Delta_n = 0$ is

given in Fig. 3.7, where $\mathcal{A}$ becomes constant at steady state, unlike when $\Delta_n \neq 0$. This is the same for all other variables (ρ_{cd} and $\mathcal{B}$) for all combinations of g, Ω_a and system parameters. Therefore, it is possible to set all time derivatives in Eq. (3.16a-3.16k) to 0, which yields a set of algebraic equations that can be solved.

$$0 = \gamma_{21}\rho_{22} + \gamma_{31}\rho_{33} - g\rho_{11} + 2\tilde{\Omega}_b B\rho_{21,R} - 2\tilde{\Omega}_b A\rho_{21,I} \tag{3.17}$$

$$0 = -(\gamma_{31} + \gamma_{32})\rho_{33} + g\rho_{11} + 2\Omega_a\rho_{32,I} \tag{3.18}$$

$$0 = -\Gamma_{21}\rho_{21,R} + \tilde{\Omega}_b B\rho_{22} - \tilde{\Omega}_b B\rho_{11} - \Omega_a\rho_{31,I} \tag{3.19}$$

$$0 = -\Gamma_{21}\rho_{21,I} - \tilde{\Omega}_b A\rho_{22} + \tilde{\Omega}_b A\rho_{11} - \Omega_a\rho_{31,R} \tag{3.20}$$

$$0 = -\Gamma_{31}\rho_{31,R} + \tilde{\Omega}_b A\rho_{32,I} + \tilde{\Omega}_b B\rho_{32,R} - \Omega_a\rho_{21,I} \tag{3.21}$$

$$0 = -\Gamma_{31}\rho_{31,I} - \tilde{\Omega}_b A\rho_{32,R} + \tilde{\Omega}_b B\rho_{32,I} + \Omega_a\rho_{21,R} \tag{3.22}$$

$$0 = -\Gamma_{32}\rho_{32,R} + \tilde{\Omega}_b A\rho_{31,I} - \tilde{\Omega}_b B\rho_{31,R} \tag{3.23}$$

$$0 = -\Gamma_{32}\rho_{32,I} - \Omega_a\rho_{33} + \Omega_a\rho_{22} - \tilde{\Omega}_b A\rho_{31,R} - \tilde{\Omega}_b B\rho_{31,I} \tag{3.24}$$

$$1 = \rho_{11} + \rho_{22} + \rho_{33} \tag{3.25}$$

$$0 = -\gamma_n A - N_c\tilde{\Omega}_b\rho_{21,I} \tag{3.26}$$

$$0 = -\gamma_n B + N_c\tilde{\Omega}_b\rho_{21,R} \tag{3.27}$$

By simultaneously solving the system of non-linear algebraic equations we derive the full explicit analytical expression for N_n as follows.

$$N_n = \left[(-8\gamma_n\mathcal{F}_5((\Gamma_{21}\Gamma_{31}\gamma_n + \gamma_n\Omega_a^2)\mathcal{F}_{10}\right.$$
$$\left. + N_c\tilde{\Omega}_b^2(\Gamma_{31}\Gamma_{32}\mathcal{F}_4 + \Omega_a^2\mathcal{F}_7)) + \mathcal{F}_8^2)^{\frac{1}{2}} - \mathcal{F}_8\right]\frac{1}{\mathcal{F}_9}, \tag{3.28}$$

where $\mathcal{F}_1 = \Gamma_{32}(2\gamma_{31} + 2\gamma_{32} + g) + 6\Omega_a^2$, $\mathcal{F}_2 = \gamma_{21}(\gamma_{31} + \gamma_{32} + g) + \gamma_{32}g$, $\mathcal{F}_3 = \gamma_{21} - 3\gamma_{31} - \gamma_{32} - 3g$, $\mathcal{F}_4 = \gamma_{21}\gamma_{31} + \gamma_{21}\gamma_{32} - \gamma_{32}g$, $\mathcal{F}_5 = 2\gamma_{31} + 2\gamma_{32} + g$, $\mathcal{F}_6 = \gamma_{21} + \gamma_{31} + 2g$, $\mathcal{F}_7 = 2\gamma_{31}\Gamma_{31} - 2\Gamma_{31}g + 2\Gamma_{31}\gamma_{21} - \gamma_{21}g$, $\mathcal{F}_8 = 2\gamma_n\Gamma_{31}\mathcal{F}_1 + \gamma_n\Gamma_{21}\mathcal{F}_2 + 2\gamma_n\Omega_a^2\mathcal{F}_3 + N_c\tilde{\Omega}_b^2\mathcal{F}_4$, $\mathcal{F}_9 = 4\gamma_n\mathcal{F}_5\tilde{\Omega}_b^2$ and $\mathcal{F}_{10} = \Gamma_{32}\mathcal{F}_2 + 2\Omega_a^2\mathcal{F}_6$. Eq.(5.19) can be used to analyze the number of SPs analytically, for $g > g_{th}$ where g_{th} is the spasing threshold. It gives a fully analytical characterization of the spasing curve since it contains both controlling parameters g and Ω_a as well as all system specific parameters. We now compare the numerical simulations with the results generated by our analytical expression for the spaser proposed in [31]. The error percentage ($\mathcal{E}$) is defined as $(N_n^s - N_n)/N_n^s \times 100\%$, where N_n^s is the value obtained in numerical simulations.

3.7.1   Comparison of numerical and analytical results

We now compare the numerical simulations with the results generated by our analytical expression for the spaser proposed in [31]. The error percentage ($\mathcal{E}$) is defined as $(N_n^s - N_n)/N_n^s \times 100\%$, where N_n^s is the value obtained in numerical simulations. In order to prove the validity of the analytical expression in Eq.5.19, we have performed a comparison of the analytical results and the numerical results. Figs. 3.8(a)-(b) depicts the spasing curve of N_n as g varies. Different curves have been obtained for various values of Ω_a. It is evident that $\mathcal{E}$ for the whole spasing regime ($g > g_{th}$) remains less than 0.1% in all practical cases [10,11,55,83]. Studying the effect of dephasing (decoherence) on spasing is also of utmost importance for a complete characterization [108]. Therefore, another comparison is made in Figs. 3.8(c)-(d) to investigate the effect of decoherence (γ_{ph}) on spasing. While it becomes evident that the robustness of the spaser output against decoherence has been enhanced as Ω_a is increased, it can also be seen that Eq. (5.19) can be used with an acceptable accuracy ($\mathcal{E} < 0.1\%$) to study the effect of
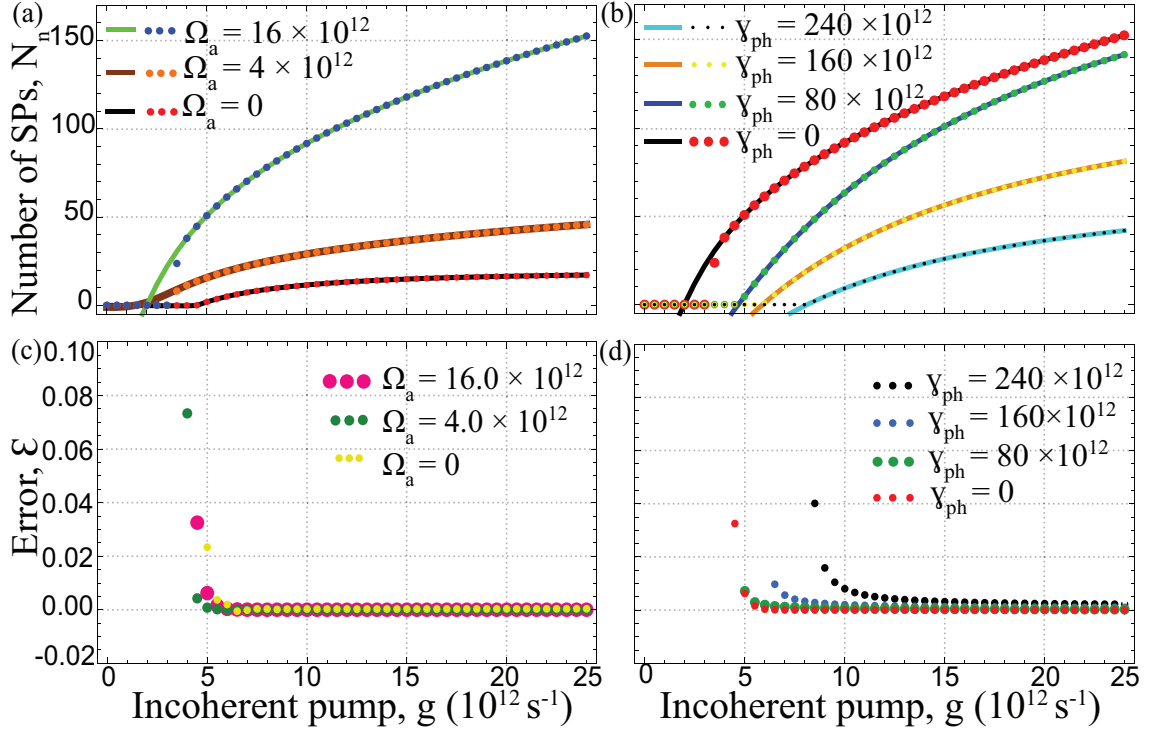
Figure 3.8: Subfigures (a)-(d) compare the spasing curves obtained both numerically and analytically. Dotted lines in (a) and (c) represent the numerical results and the solid lines represent our analytical results. (a) shows the spasing curves obtained both numerically and analytically for different values of Ω_a where $\gamma_{ph} = 0$ for all cases. The corresponding error ($\mathcal{E}$) values are shown in (c). (b) shows the spasing curves obtained both numerically and analytically for different values of γ_{ph} where $\Omega_a = 16x10^{12}s^{-1}$ for all cases. The corresponding error ($\mathcal{E}$) values are shown in (d). Percentage error ($\mathcal{E}$) is less than 0.1% for all cases in the spasing regime ($g > g_{th}$).

dissipative processes such as decoherence (γ_{ph}) in a spaser.

3.8   Physical insights

We have ideally assumed a pure state initial condition for the density matrix elements when obtaining numerical results. There is a slight disagreement between the numerical and analytical results for very small g values above the threshold, for high Ω_a. This could be due to the inability of the system to produce the ex-
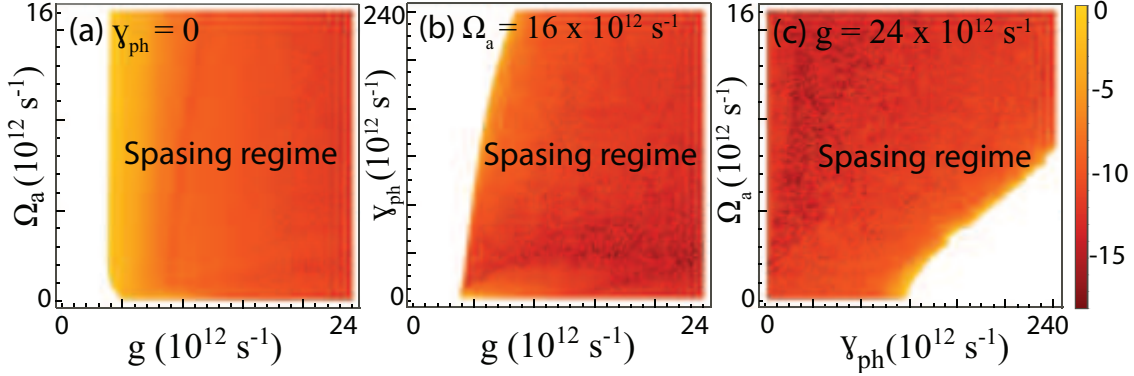
Figure 3.9: Subfigures (a)-(c) depict the two-dimensional plots for the logarithmic value of the absolute value of the error ($\mathcal{E}$) percentage. (a) shows $\log_{10}(|\mathcal{E}|)$ for a range of values of g and Ω_a when $\gamma_{ph} = 0$. (b) shows $\log_{10}(|\mathcal{E}|)$ for a range of values of g and γ_{ph} when $\Omega_a = 16 \times 10^{12}s^{-1}$. (c) shows $\log_{10}(|\mathcal{E}|)$ for a range of values of Ω_a and γ_{ph} when $g = 24 \times 10^{12}s^{-1}$. Error ($\mathcal{E}$) is less than 0.1% for all cases in the spasing regime. Non-spasing regimes are shown in white.

pected response to the high Ω_a values at very low pumping rates, as the number of electrons in high energy levels are minute in the initial spasing build up. If a more practical mixed initial state is assumed instead [3, 34], even this slight disagreement will no longer be present due to the initial presence of electrons in the upper energy levels to compensate for the low pumping rates. Furthermore, for practical pumping rates so far reported in literature ($g > 5 \times 10^{12}\,\mathrm{s}^{-1}$) [10, 11, 55, 83], the values obtained using both types of initial conditions converge to our steady state analytical solution. Fig. 3.8 and 3.9 also suggest that apart from accurately characterizing the spaser output with $\mathcal{E} < 0.1\%$ for $g > g_{th}$ when $\Delta_n \ll \gamma_n, \omega_n$, it is also possible to use Eq. (5.19) to qualitatively understand the threshold conditions (g_{th}) by setting $N_n = 0$. When Δ_n is comparable or greater than ω_n or γ_n, the predicted analytical values will not be within the accepted error bounds, i.e. $\mathcal{E} > 0.1\%$. But such off-resonant conditions are not desired practically from a system designer's perspective since such conditions do not facilitate efficient energy transfer and there is some likelihood for system instability as well [18].

Eq.(5.19) can be tailored for different nano-particles and gain media by varying $\tilde{\Omega}_b$, decay and dephasing rates and N_c accordingly. It is also possible to derive simpler expressions when the parameters are constrained to specific regimes. For example, if a certain spaser configuration satisfies the condition $g > \gamma_{21} \gg \gamma_{32} \gg \gamma_{31}$, its spasing curve can be derived in a more simplified form as follows:

$$
\begin{aligned}
N_n \approx {} & \frac{\gamma_{32} N_c}{4\gamma_n} \left(1 - \frac{\gamma_{21}}{g}\right) - \frac{\gamma_{21}}{4\tilde{\Omega}_b^2} \left(g + \frac{2\Omega_a^2}{g}\right) \\
& + \frac{1}{4} \left[\left(1 - \frac{\gamma_{21}}{g}\right)^2 \left(\frac{\gamma_{32} N_c}{\gamma_n}\right)^2 + \frac{8g N_c \Omega_a^2}{\gamma_n}\right]^{\frac{1}{2}}.
\end{aligned}
\tag{3.29}
$$

To simply model the main physical dependencies of the system, we considered the Taylor series expansion of Eq. (5.19) for the whole operating regime for fixed values of Ω_a. We could approximate that N_n shows a logarithmic behavior as g varies, expressed as

$$
k_1 \ln(g - k_2 g_{th}),
\tag{3.30}
$$

where k_1 and k_2 depend on system parameters and Ω_a. Similar analyses can be done to simply approximate the relationships between other parameters.

3.8.1 Design optimization

Eq.(5.19) can be used to analytically study the relationship between any selected pair of parameters by setting others as constants, similar to the way it is done for g vs. N_n. To demonstrate the versatility of our solution, we have studied how N_n behaves as the number of chromophores (N_c) is varied in Fig. 3.10-(a). Then we set $N_n = 0$ in Eq. (5.19) and express the threshold number of chromophores $N_{c,th}$ as a function of Ω_a, depicted in Fig.3.10-(b). Such analyses for any set of parameters can be performed using our analytical solution. This enables the system designers to develop highly intuitive and methodical optimization schemes
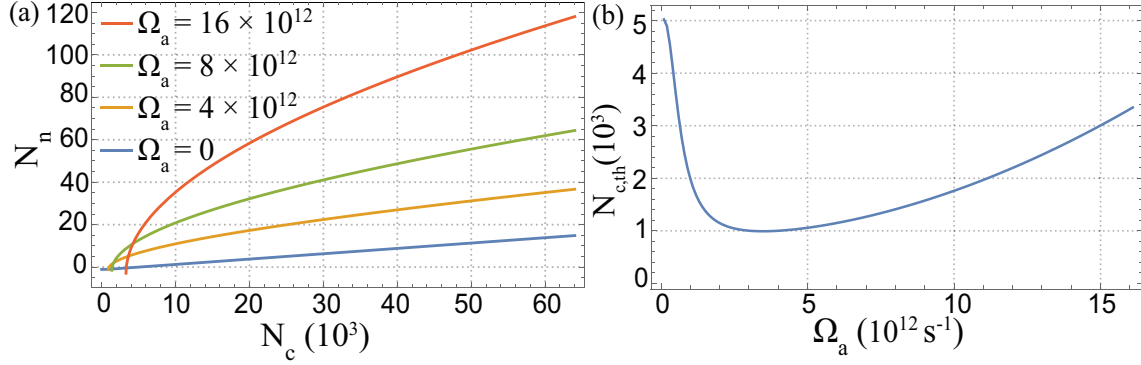
Figure 3.10: (a) depicts the variation of N_n as N_c varies for different values of Ω_a. (b) shows the variation of minimum N_c (threshold) required to start spasing ($N_{c,th}$) as Ω_a varies in the configuration given in (a). Note that $g = 15 \times 10^{12}\,\text{s}^{-1}$ and $\gamma_{ph} = 0$ for both (a) and (b).

for physically meaningful parameter sets, which is much simpler than full-blown numerical approaches. In addition, by setting $\Omega_a = 0$ and $\gamma_{32} > g$ in Eq. (5.19) for a much faster $|3\rangle \to |2\rangle$ population transfer [31], it is possible to study the spasing output of a 2-level spaser [11] analytically.

3.9   Spasing frequency

The spasing frequency (v_s) can be found with the equations (3.17-3.27) along with the spasing condition presented in [18], as follows:

$$v_s = \frac{\alpha \omega_{21} + \mathcal{K}_s \omega_n}{\alpha + \mathcal{K}_s},\tag{3.31}$$

where $\mathcal{K}_s = (0.5(\gamma_{21} + g) + \gamma_{ph})(0.5(\gamma_{31} + \gamma_{32} + g) + \gamma_{ph}) + \Omega_a^2$ and

$$\alpha = [(N_c \tilde{\Omega}_b^2 / \Gamma_{32} \tilde{\Gamma}_{31}) n_{32} - \gamma_n / \tilde{\Gamma}_{31}]\Omega_a^2 + \gamma_n \tilde{\Gamma}_{31}.\tag{3.32}$$

Note that $\tilde{\Gamma}_{ij} = \text{Re}(\Gamma_{ij})$ and n_{32} is the corresponding population inversion. Eq. 3.31 is obtained under the assumption of $\Omega_b \ll \Omega_a$ [31].

Eq. 3.31 shows that v_s depends on Ω_a. That means we can use the additional coherent electric field Ω_a to control the spasing frequency up to a considerable extent. This is another advantage of the three-level model. In the conventional two-level system, it is not possible to tune the spasing frequency dynamically, when the system configuration is set. The three-level model provides a considerable amount of tunability.

3.10 Conclusion

In conclusion, we have derived an explicit analytical expression and simpler approximations to describe the spasing curves of a coherently enhanced spaser, whilst providing valuable physical insights into the operation of the spaser. The method we have followed in deriving the solution itself will aid similar nano-plasmonic systems to be solved analytically to a very high accuracy. The derived expression provides the basis to calculate the optimal system parameters and inputs required in order to achieve desired spasing outputs, which is a capability that surpasses numerical solutions. Therefore, the proposed scheme enables the utilization of spasers in complex nano-plasmonic systems by enabling design optimization. In addition, it grants a faster way to determine the output energy generated by the localized SPs, eliminating the need of computationally expensive numerical simulations. The error of the spasing curve generated by our expression is under 0.1% for the whole operating regime above the spasing threshold, suggesting an almost perfect characterization.

This page intentionally left blank.

Chapter 4

Analytical characterization of spasing threshold

In the study we report in this chapter, we target spasing threshold as one of the key output characteristics that require close attention. Given the recent experimental success in demonstrating the operation of the three-level spaser, we consider the analytical approach we present here to study the spasing threshold is topical and would enable many promising applications in nanoplasmonics.

4.1 Introduction

The spasing curve of a 3-level spaser has been analytically quantified in [113], providing guidelines for design optimization. This breakthrough was reported in Chapter 3 of this thesis. Less than half a decade since the concept has been theorized, in 2018, the first experimental realization of a 3-level spaser system has been accomplished by Song *et al.* [27], accelerating the progress of spaser technology.

As a natural continuation of the previous chapter, we then analyse the effects of the 3-level model of chromophores and the impact of the additional coherent optical field on the spasing threshold and the minimum pumping requirements. We obtain an analytical expression for the spasing threshold of a 3-level spaser, which explains how the threshold changes when all system specific parameters

are varied. We also derive simpler expressions, which provide better physical insights into the operation of the device. We then proceed to observe the population inversion at spasing threshold and the population densities of each level to describe the effects of incoherent pumping as well as the coherent drive. Furthermore, we establish a phenomena analogous to lasing without inversion in 3-level spasers. In addition, we study the extreme limits of the coherent drive, which maintains the threshold pumping requirements at a lower value compared to a conventional two-level spaser. The effect of decoherence (phase relaxation) on the spasing threshold will also be investigated. We also prove that our approach can lead to the threshold conditions of a two-level spaser, further verifying the validity of the solution.

4.2 Theoretical formalism

4.2.1 Basic Configuration

The basic configuration and the energy flow diagram depicting the spasing process is shown in Fig. 4.1. The same model presented in chapter 3 will be used. For the ease of following the material, we present a brief overview of the system.

Each emitter has 3 states, namely a ground state ($|1\rangle$) and two excited states ($|2\rangle$ and $|3\rangle$), respectively. Two inputs are provided to power up the spaser. They are denoted by the incoherent pumping rate (g) and the Rabi frequency of a coherent optical field Ω_a. As illustrated in Fig. 4.1, g is coupled with the transition $|1\rangle \rightarrow |3\rangle$, and Ω_a is coupled with the transition $|2\rangle \rightarrow |3\rangle$.

The gain medium surrounds a plasmonic nano-resonator, which is the other main component of the system. The spasing transition ($|2\rangle \rightarrow |1\rangle$) of the gain medium is coupled with a SP mode in the nano-plasmonic resonator and the coupling term is represented by the corresponding Rabi frequency Ω_b. As the

system is continuously powered via g and Ω_a, the spasing transition transfers energy non-radiatively to the SP mode, and the generated plasmonic field provides a feedback in turn, into the gain medium, thereby arriving at an equilibrium to sustain the spasing process. The spontaneous decay rates in the 3-level emitters are denoted by γ_{21}, γ_{32} and γ_{31}. The total number of 3-level quantum emitters (chromophores) in the gain medium is denoted by N_c.

4.2.2 Mathematical model

The basic principles, the model and notations are similar to that of chapter 3. Surface plasmons are modelled using $\mathbb{C}$-numbers corresponding to bosonic number state representation where N_n denotes the expected number of SPs generated in the spasing mode with frequency ω_n [110]. The total power output of the spaser is then given by $\hbar\omega_n \times N_n$. Hence, N_n gives a measure of the total output power of the spaser, where $N_n = |a_{0_n}|^2$ and $|a_{0_n}|^2 = \mathcal{A}^2 + \mathcal{B}^2$. Therefore, the values of $\mathcal{A}$ and $\mathcal{B}$ will be of significant importance in our calculations to arrive at various properties describing the spasing threshold.

4.2.3 Spasing threshold

As one of the major contributions of this chapter, we derive analytical expressions for parameters such as the incoherent pumping rate (g), population densities (ρ_{cc}'s), population inversions ($n_{21} = \rho_{22} - \rho_{11}$ and $n_{32} = \rho_{33} - \rho_{22}$) and the off diagonal components of the density matrix (ρ_{cd}'s where $c \neq d$) at the spasing threshold.

The condition for spasing is taken as $N_n \geq 0$ [18]. The equality, i.e. $N_n = 0$ occurs at the spasing threshold. In other words, when we keep on increasing the incoherent pumping rate (g) from zero, the point at which the spaser just starts generating a constant plasmonic field is considered as the spasing threshold. It
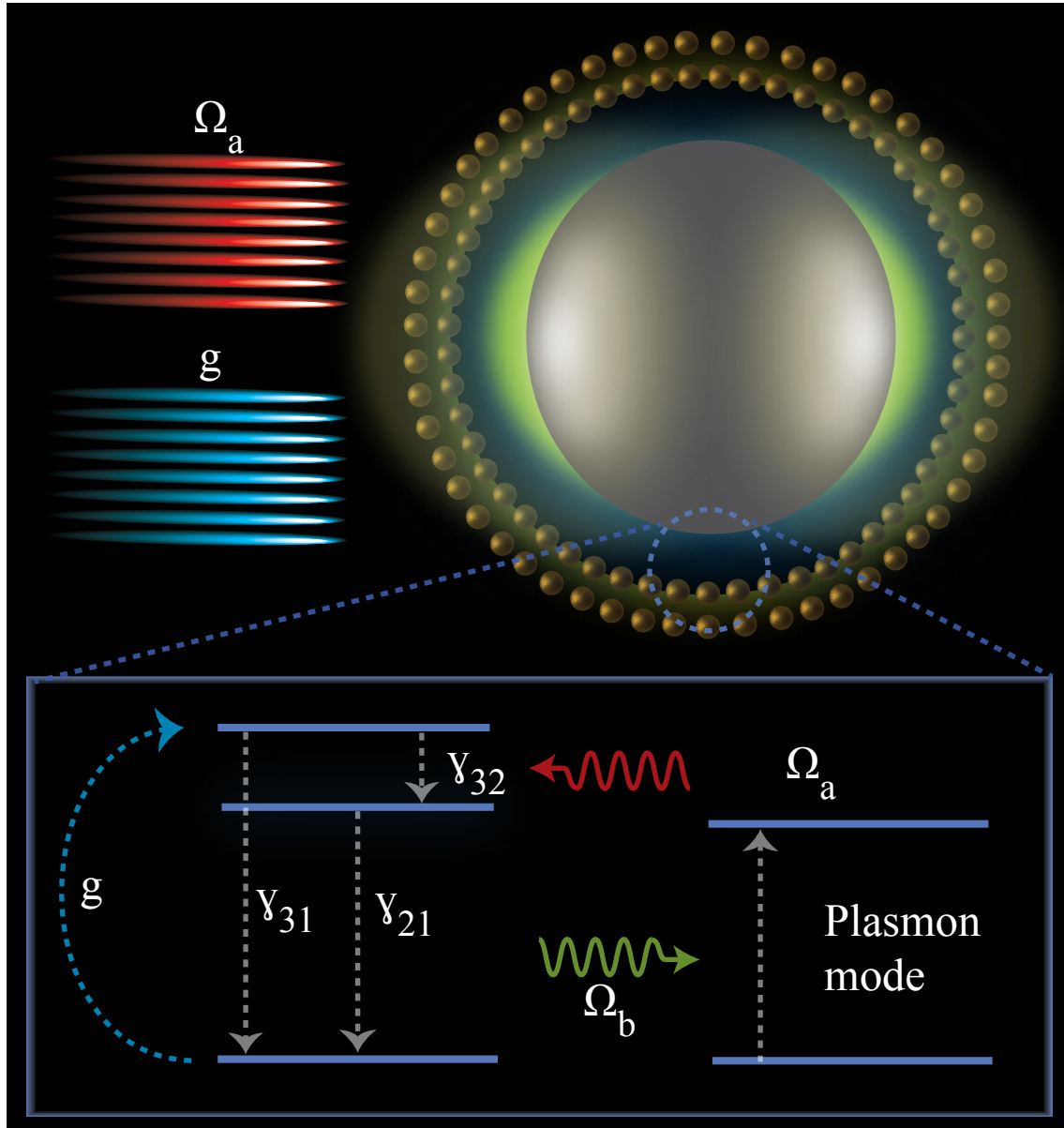
Figure 4.1: Basic operation of a spaser: Gain medium chromophores are excited using an incoherent pump (g) as well as a coherent drive Ω_a. The transition $|2\rangle \to |1\rangle$ is coupled to one of the SP modes in the plasmonic nano-structure, which excites SPs via stimulated emission.

can also be seen as the point where the gain due to stimulated emission becomes dominant compared to the loss due to plasmonic decay [19]. After that point, the plasmon annihilation operator (a_{0n}) starts to have a positive value. Therefore, at spasing threshold, which is the limiting point that seperates the spasing regime and the non-spasing regime, we take $a_{0n} = 0$. Therefore, $\mathcal{A} = 0$ and $\mathcal{B} = 0$.

Moreover, since we are solving equations (3.16a - 3.16k) at the spasing threshold, we change the notation of each variable with the subscript "th". For example, $\mathrm{Re}(\rho_{21})$, which is denoted as ρ_{21}^R becomes $\rho_{21,th}^R$ at threshold. $\mathrm{Im}(\rho_{21})$, which is denoted as ρ_{21}^I becomes $\rho_{21,th}^I$ at threshold, etc. The minimum value of the incoherent pumping rate required to start spasing is denoted as (g_m).

After the initial transients in the time domain, the output power of the spaser (represented by N_n) gets settled into a constant value only in the steady state regime for a given set of inputs, as indicated in [10, 11, 113]. Therefore, we simultaneously solve equations (3.16a - 3.16k) for the steady state operation of the spaser, after the initial transients are over, where all time derivatives become zero.

Solving Eq. (3.16a - 3.16k) yields $\rho_{21,th}^R = 0$, $\rho_{21,th}^I = 0$, $\rho_{31,th}^R = 0$, $\rho_{31,th}^I = 0$ and $\rho_{32,th}^R = 0$. Further, we obtain a simpler set of equations as follows:

$$0 = \gamma_{21}\rho_{22,th} + \gamma_{31}\rho_{33,th} - g_m\rho_{11,th} \tag{4.1}$$

$$0 = -(\gamma_{31} + \gamma_{32})\rho_{33,th} + g_m\rho_{11,th} + 2\Omega_a\rho_{32,th}^I \tag{4.2}$$

$$0 = \Omega_a(\rho_{22,th} - \rho_{33,th}) - \Gamma_{32}\rho_{32,th}^I \tag{4.3}$$

$$\rho_{11,th} = 1 - \rho_{22,th} - \rho_{33,th}. \tag{4.4}$$

By solving equations (4.1-4.4) simultaneously, we derive the following results, which describe some of the crucial physical parameters at the spasing threshold:

$$\rho_{11,th} = \frac{1}{D_1}\left(\Gamma_{32}\gamma_{21}\gamma_{31} + \Gamma_{32}\gamma_{21}\gamma_{32} + 2\gamma_{21}\Omega_a^2 + 2\gamma_{31}\Omega_a^2\right) \tag{4.5}$$

$$\rho_{22,\text{th}} = \frac{g_m}{D_1}\left(\Gamma_{32}\gamma_{32} + 2\Omega_a^2\right) \tag{4.6}$$

$$\rho_{33,\text{th}} = \frac{g_m}{D_1}\left(\Gamma_{32}\gamma_{21} + 2\Omega_a^2\right) \tag{4.7}$$

$$\rho_{32,\text{th}}^{\text{I}} = \frac{\Omega_a g_m}{D_1}\left(\gamma_{32} - \gamma_{21}\right), \tag{4.8}$$

where $D_1 = \Gamma_{32}\gamma_{21}\gamma_{31} + \Gamma_{32}\gamma_{21}\gamma_{32} + \Gamma_{32}\gamma_{21}g_m + \Gamma_{32}\gamma_{32}g_m + 2\gamma_{21}\Omega_a^2 + 2\gamma_{31}\Omega_a^2 + 4g_m\Omega_a^2$. Equations (4.5-4.7) describe the population probabilities at the threshold, which are quite essential in understanding the physics of the initial build up of spasing. For instance, according to Eq. 4.6 and Eq. 4.7, even in the presence of Ω_a, the populations ρ_{22} and ρ_{33} will stay at zero when the incoherent pumping (g) is not present, meaning that the chromophores will not be excited.

According to Eq. 4.8, since the density matrix describing the spaser operation at threshold has one non-zero off-diagonal term, i.e. $\rho_{32,\text{th}}^{\text{I}}$, the coherence between states $|3\rangle$ and $|2\rangle$ will be maintained only at the presence of non-zero g and Ω_a. Note that $\rho_{32,\text{th}} = \rho_{32,\text{th}}^{\text{I}}$ since it was earlier shown that $\rho_{32,\text{th}}^{\text{R}} = 0$. Furthermore, using Eq. 4.7 and Eq. 4.6, we calculate the population inversion between $|3\rangle$ and $|2\rangle$, which is $\rho_{33,\text{th}} - \rho_{22,\text{th}}$, as,

$$n_{32,\text{th}} = \frac{g_m\Gamma_{32}\left(\gamma_{21} - \gamma_{32}\right)}{\mathcal{D}_1} \tag{4.9}$$

Equation 4.9 suggests that a positive population inversion will always be present as long as $\gamma_{21} > \gamma_{32}$. In conventional 2-level spaser designs, the two level atoms are modelled to have extremely high decay rates from the higher energy levels to the second energy level $|2\rangle$, i.e. $\gamma_{32} \gg \gamma_{21}$ [11]. In such cases, $n_{32,\text{th}}$ becomes negative. On the other hand, when modelling the 3-level gain mediums, it has been considered that $\gamma_{32} < \gamma_{21}$ [113]. Hence, Eq. 4.9, which we have derived, suggests that $n_{32,\text{th}} > 0$ for the spaser to start operation.

Population inversion in the spasing transition ($|2\rangle \rightarrow |1\rangle$) at the threshold, $n_{21,\text{th}}$, and the overall inversion at the threshold, $\eta_{\text{th}} = \rho_{33,\text{th}} + \rho_{22,\text{th}} - \rho_{11,\text{th}}$, can

be derived from Eq. (4.5 - 4.7) as,

$$\mathcal{D}_1 n_{21,\text{th}} = 2\Omega_a^2 \left(g_\text{m} - 2(\gamma_{21} + \gamma_{31})\right) + \Gamma_{32} \left(\gamma_{32} g_\text{m} - \gamma_{21}(\gamma_{32} + \gamma_{31})\right), \quad (4.10)$$

$$\mathcal{D}_1 \eta_\text{th} = 2\Omega_a^2 \left(2g_\text{m} - (\gamma_{21} + \gamma_{31})\right) + \Gamma_{32} \left(g_\text{m}(\gamma_{21} + \gamma_{32}) - \gamma_{21}(\gamma_{31} + \gamma_{32})\right).$$
$$(4.11)$$

Using the derived expressions and by referring to the decay rates and typical minimum pumping rates reported in literature [18, 31, 113], we can show that $\eta_\text{th} > 0$ and $n_{21,\text{th}} < 0$ in the vicinity of the spasing threshold for a major part of the operating regime. These rigorous derivations go in line with the previously demonstrated numerical simulations of 3-level spasers in chapter 3 as well. Usually, in 2-level spasers, $n_{21,\text{th}}$ should be positive to start spasing, which suggests that, in 3-level spasers, spasing starts even before the population is inverted in the spasing transition. It is an analogous phenomena to lasing without inversion (LWI) in macroscopic lasers [114]. As the next step, we derive the minimum value of the incoherent pumping rate required to start spasing (g_m), analytically. During the earlier derivations for Eq. 4.5-4.8, we set $\mathcal{A}, \mathcal{B} = 0$. Since it reduces the original system of differential equations from Eq. (3.16a-3.16k) to Eq. (4.1-4.4), using the earlier approach, it is not possible to derive a value for g_m independent of the population densities, $\rho_{11,\text{th}}, \rho_{22,\text{th}}$ and $\rho_{33,\text{th}}$. Our objective here is to derive an expression for g_m in terms of the system specific parameters and the other input, Ω_a, such that it enables us to study the possibility of controlling g_m independent of the threshold population densities of the device. Hence, as the first step, we now make the plasmon annihilation operator's real part equal to zero, i.e. $\text{Re}(a_{0\text{n}}) = \mathcal{A} = 0$, and solve equations (3.16a-3.16k) simultaneously for the steady state operation of the spaser, and secondly, let $\mathcal{B} = 0$, to obtain the
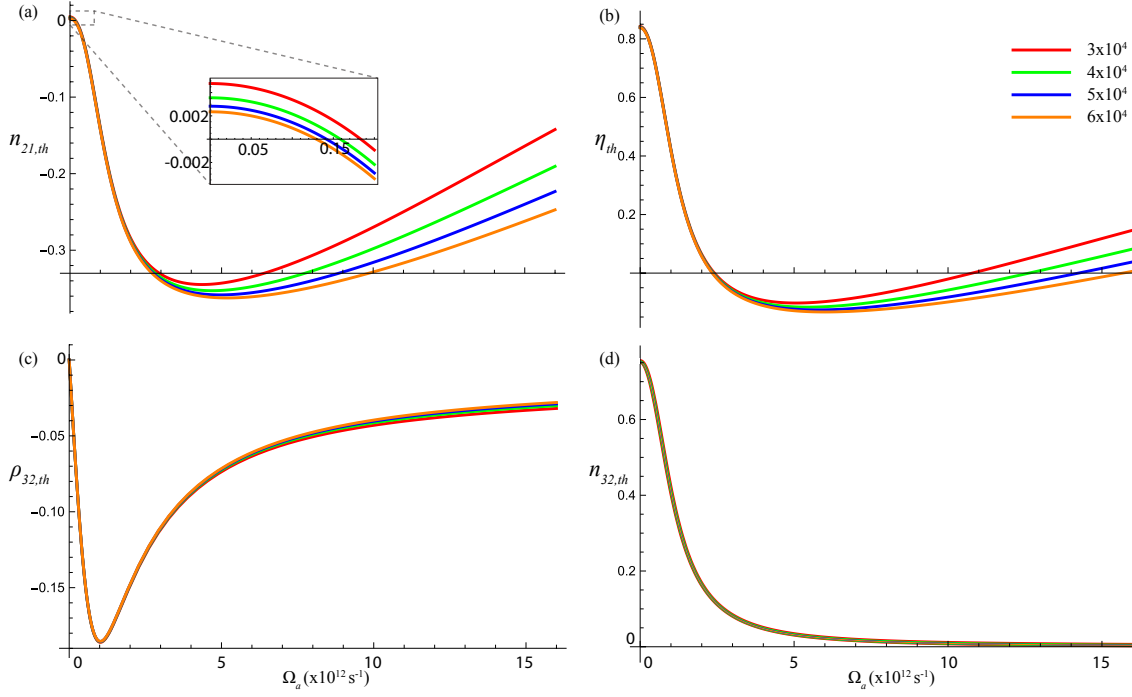
Figure 4.2: (a) shows the behavior of the population inversion n_{21} of the spasing transition at spasing threshold as the coherent drive (Ω_a) varies, for different values of N_c. The zoomed in figure in subfigure (a) shows how n_{21} at the threshold remains positive for very small values of Ω_a. (b) shows how the overall inversion (η) at the spasing threshold varies, as the coherent drive (Ω_a) changes, for different values of N_c. (c) shows the variation of ρ_{32}^I versus Ω_a for different values of N_c. (d) shows the behavior of n_{32} as Ω_a changes, for different values of N_c. The legends indicated in subfigure (b) is the same for all 4 subfigures. In all cases, the decoherence rate (γ_{ph}) remains a constant at zero.

following expression for g_m.

$$g_m = \frac{\mathcal{K}_2 \left(\Gamma_{21}\Gamma_{31}\gamma_n + \gamma_n\Omega_a^2 + \Gamma_{31}N_c\tilde{\Omega}_b^2\right)}{N_c\tilde{\Omega}_b^2 \left(\Gamma_{31}\Gamma_{32}\gamma_{32} + (2\Gamma_{31} + \gamma_{21} - \gamma_{32})\Omega_a^2\right) - \gamma_n\mathcal{K}_1 \left(\Gamma_{21}\Gamma_{31} + \Omega_a^2\right)}, \quad (4.12)$$

where $\mathcal{K}_1 = \Gamma_{32}(\gamma_{21} + \gamma_{32}) + 4\Omega_a^2$ and $\mathcal{K}_2 = \Gamma_{32}\gamma_{21}(\gamma_{31} + \gamma_{32}) + 2(\gamma_{21} + \gamma_{31})\Omega_a^2$. As per Eq. (3.6-3.8), Γ_{21} and Γ_{31} are dependant on g. Therefore, the right hand side of Eq.4.12 is again a function of g_m itself. Hence, in order to get rid of this dependency, we rearrange Eq.4.12 and write it as a cubic equation of g_m as,

$$\mathcal{C}_3 g_m^3 + \mathcal{C}_2 g_m^2 + \mathcal{C}_1 g_m + \mathcal{C}_0 = 0. \quad (4.13)$$

The real-valued coefficients $\mathcal{C}_0, \mathcal{C}_1, \mathcal{C}_2$ and $\mathcal{C}_3$ can be derived as follows. We consider that the rate of decoherence (phase relaxation) is neglegible in our derivation, i.e. $\gamma_{ph} \approx 0$.

$$\mathcal{C}_0 = \frac{1}{4} \left(\gamma_{21}\gamma_n\mathcal{K}_2(\gamma_{31} + \gamma_{32}) + 4\gamma_n\mathcal{K}_2\Omega_a^2 + 2\mathcal{K}_2 N_p\tilde{\Omega}_b^2(\gamma_{31} + \gamma_{32}) \right), \quad (4.14)$$

$$4\mathcal{C}_1 = \gamma_{21}\gamma_n\mathcal{K}_1(\gamma_{31} + \gamma_{32}) + 2\gamma_n\mathcal{K}_2\Gamma_{32} + 4\gamma_n\mathcal{K}_1\Omega_a^2$$
$$- 2\gamma_{32}N_c\tilde{\Omega}_b^2\Gamma_{32}(\gamma_{31} + \gamma_{32}) + 2\mathcal{K}_2 N_c\tilde{\Omega}_b^2 - 4N_c\Omega_a^2\tilde{\Omega}_b^2(\gamma_{21} + \gamma_{21}), \quad (4.15)$$

$$\mathcal{C}_2 = \frac{1}{4} \left(2\gamma_n\mathcal{K}_1\Gamma_{32} + \gamma_n\mathcal{K}_2 - 2\gamma_{32}\Gamma_{32}N_c\tilde{\Omega}_b^2 - 4N_p\Omega_a^2\tilde{\Omega}_b^2 \right), \quad (4.16)$$

$$\mathcal{C}_3 = \frac{1}{4}\gamma_n\mathcal{K}_1. \quad (4.17)$$

Solving Eq. 4.13 using the derived coefficient values for $\mathcal{C}_0, \mathcal{C}_1, \mathcal{C}_2$ and $\mathcal{C}_3$ provides us with an explicit analytical expression for g_m which enables us to comprehensively study the input power requirements to achieve spasing in 3-level spasers. According to Eq. (4.14-4.17), $\mathcal{C}_0, \mathcal{C}_1, \mathcal{C}_2$ and $\mathcal{C}_3$ contain all system specific parameters as well as Ω_a, which provides us with an explicit analytical solution for g_m of a 3-level spaser.

Furthermore, for the special case of $\Omega_a = 0$, using Eq. 5.1, we derive the minimum incoherent pumping rate required to start spasing as,

$$g_m|_{\Omega_a=0} \approx \gamma_{21}\left(1 + \frac{\gamma_{31}}{\gamma_{32}}\right). \tag{4.18}$$

It can be further simplified to obtain the minimum incoherent pumping rate of a 2-level spaser by assuming $\gamma_{32} \gg \gamma_{21}, \gamma_{31}$ [31,113] as,

$$g_{m,2} \approx \gamma_{21}, \tag{4.19}$$

which closely resembles the observed minimum values for the incoherent pumping rate [10,11,115] to start a 2-level spaser. This further verifies that our approach and the solutions that have been derived are accurate, and can be used to describe the various physical properties of a spaser at spasing threshold.

4.2.4   Threshold Gain

Plasmonic nano-resonator of the spaser starts generating coherent electric fields when the stimulated emission of SPs become dominant compared to the spontaneous decay of SPs. In order to quantify this further, a dimensionless gain of the nth SP mode (α_n) has been defined in [19] as $(A_n - \gamma_n)/\gamma_n$, where A_n is the Einstein coefficient which describes the net stimulated emission of SPs as,

$$A_n = \frac{4\pi}{3\hbar} \frac{s'_n s_n |d_{12}|^2 p_n q_n}{\epsilon_d (\text{Im}[s(\omega_n)])^2} \gamma_n. \tag{4.20}$$

p_n is the spatial overlap factor between the population inversion and SP mode intensity given by $\int [\rho_{22}(r) - \rho_{11}(r)] \times [\nabla\psi_n(r)]^2 d^3r$, where $[\nabla\psi_n(r)]^2 \approx 1/V_n$. V_n is the mode volume of the nth SP mode. Since we assumed earlier that all gain chromophores interact with the SP mode identically, we omit the r dependency and write $\rho_{22}(r) - \rho_{11}(r)$ as n_{21} to be consistent with the notation we adopt in

our work. All other variables have the usual definitions as in [18, 19]. Quantum generation of SPs exists only if $\alpha_n \geq 0$, i.e.,

$$A_n \geq \gamma_n. \tag{4.21}$$

However, due to the phenomena of spasing without inversion in three-level spasers, population inversion of the spasing transition at threshold ($n_{21,\text{th}}$) remains negative. Consequently, the spatial overlap factor, p_n should be adjusted to suit the three-level case, to be consistent with the gain requirement in Eq. 4.21. Therefore, we modify the n_{21} term in p_n by $F(\Omega_a)n_{21}$, where $-1 \leq F(\Omega_a) \leq 1$. It is a normalized, dimensionless function of Ω_a. $F(\Omega_a)$ at spasing threshold for a three-level spaser can be obtained with the use of Eq. 5.1 and Eq. 4.21.

Furthermore, in [18], Stockman has used a gain value (G) to describe the gain medium, which has the dimensionality cm^{-1}. In his work, using the above definitions provided in [19], it has been shown that the threshold gain of the gain medium (G_{th}) for a two-level spaser depends only on the dielectric properties of the system and spasing frequency. However, for the three level case, since we showed that it is required to modify p_n by a factor of $F(\Omega_a)$, the threshold gain of the gain medium, G_{th} depends on the additional coherent drive (Ω_a) as well. Since Ω_a affects the coherence of states in the gain medium chromophores, modelling G_{th} with an Ω_a dependency is quite justifiable and intuitive.

4.3 Numerical Simulations

4.3.1 Simulation Parameters

In this section, we specify the values we use for the parameters in our numerical analysis, in order to study the analytical expressions we have derived in detail
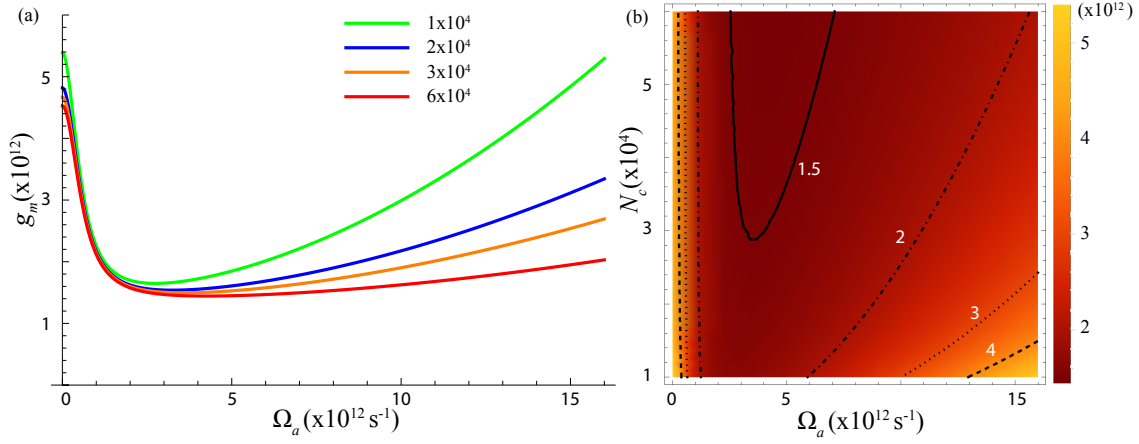
Figure 4.3: (a) shows variation of the minimum incoherent pumping rate required to start spasing (g_m) as the coherent drive (Ω_a) varies, for different values of N_c. (b) shows the top view of the color coded surface plots which depicts the minimum incoherent pumping rate to start spasing (g_m), for a large range of Ω_a and N_c. The line plots in subfigure (b) are the contour lines for different values of g_m. In all cases, the decoherence rate (γ_{ph}) remains a constant at zero. The values describing the contour plots in subfigure (b) should be scaled by a factor of $10^{12}s^{-1}$.

and also for increasing the reproducibility of our work. A silver nano-sphere of radius 40 nm is used as the plasmonic nano-structure. All parameter values are taken from [11, 31, 70, 111], where the plasmon resonance frequency (ω_n) and the plasmon decay rate (γ_n) are taken as $2.5eV$ and $5.3 \times 10^{14}s^{-1}$ respectively. As the gain medium, a generic set of quantum emitters is used with decay rates, $\gamma_{21} = 4 \times 10^{12}s^{-1}$, $\gamma_{32} = 4 \times 10^{11}s^{-1}$ and $\gamma_{31} = 4 \times 10^{10}s^{-1}$. The relative permittivity of the submerging dielectric medium is taken as $\epsilon_d = 2.25$, as in [31]. The bulk permittivity values of silver are obtained from the Johnson and Christy model [70]. In the analysis that follows, we use these as our default parameters unless mentioned otherwise.

4.3.2 Spasing without inversion

Figure 4.2 elucidates the behaviors of $n_{21,\text{th}}$, η_{th}, $\rho_{32,\text{th}}$ and $n_{32,\text{th}}$ at the spasing threshold. Fig.4.2(a) shows that for the entire operating regime of Ω_a, except for a quite small interval near zero, the population inversion of the spasing transition at threshold is negative. This suggests that it is not essential for $n_{21,\text{th}}$ at the spasing threshold to be positive for the spasing operation to start, which is an analogous phenomena to lasing without inversion (LWI) in macroscopic lasers [31]. The comparatively minute range of values of Ω_a near zero where $n_{21,\text{th}}$ remains positive suggests that for much weaker values of the coherent drive ($\Omega_a \ll \gamma_{21}$), the populations of the spasing transition are still needed to be inverted for spasing to commence.

When the spasing transition, $|2\rangle \rightarrow |1\rangle$, is considered alone, as the coherent drive Ω_a gets stronger, in Fig. 4.2(a), we observe the phenomena spasing without inversion (SWI). Figure 4.2(b) shows the variation of the overall inversion η_{th} at threshold. It suggests that the overall inversion still remains positive for a considerable portion of the operating regime for the spaser to start. This is due to the stronger coherent superposition of the two states $|3\rangle$ and $|2\rangle$. This is described by the non-zero off diagonal term of the density matrix $\rho_{32,\text{th}}$ getting stronger as Ω_a gets stronger, as demonstrated in Fig. 4.2(c). Figure 4.2 further suggests that as the number of gain medium chromophores (N_c) gets increased, both $n_{21,\text{th}}$ and η_{th} get decreased, suggesting much lower minimum pumping requirements.

4.3.3 Reduction of the threshold pumping requirements

Due to the phenomena of spasing without inversion that occurs due to the coherent drive Ω_a, it is intuitive that the minimum incoherent pumping rate requirements to start spasing would be less, compared to a conventional 2-level spaser setup where $\Omega_a = 0$. To perform a comprehensive investigation on the effect of
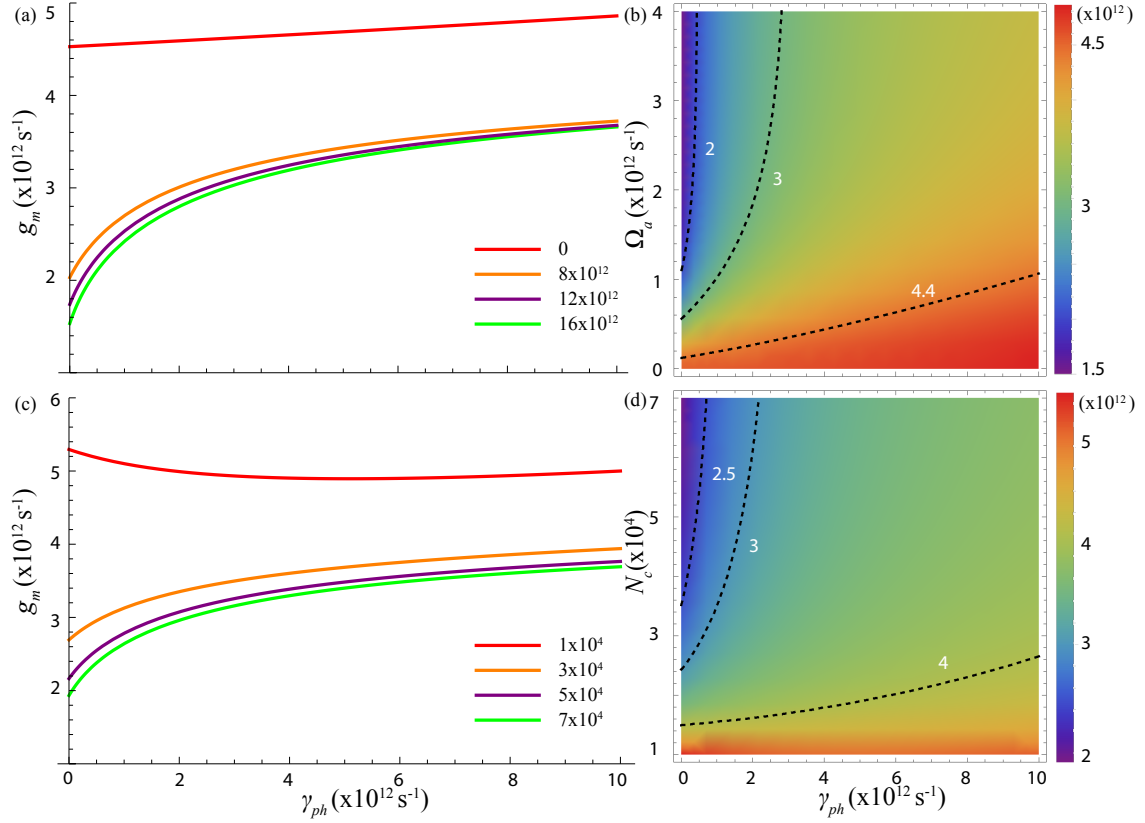
Figure 4.4: (a) shows the line plots which illustrates the behavior of the minimum incoherent pumping rate (g_{m}) required to start spasing, as the rate of decoherence (γ_{ph}) varies, for different values of Ω_a, where $N_{\mathrm{c}} = 60000$ for all line plots. (c) depicts the line plots which illustrate the behavior of g_{m} as the rate of decoherence (γ_{ph}) varies, for different values of N_{c}, where $\Omega_a = 16 \times 10^{12} s^{-1}$ for all line plots. (b) and (d) show the corresponding g_{m} values in color coded surface plots. The dotted lines in (b) and (d) show the contour lines for constant values of g_{m}. The values describing the contour plots in subfigures (b) and (d) should be scaled by a factor of $10^{12} s^{-1}$.

Ω_a on g_m, we use the derived cubic equation for g_m in Eq. 4.13 and solve for g_m with the use of coefficients, $\mathcal{C}_0, \mathcal{C}_1, \mathcal{C}_2$ and $\mathcal{C}_3$, obtained from Eq. (4.14-4.17). Since the coefficients $\mathcal{C}_0, \mathcal{C}_1, \mathcal{C}_2$ and $\mathcal{C}_3$ contain all system specific information such as the coherent drive, decay rates, number of chromophores etc., it is possible to study the dependance of minimum incoherent pumping rate required to start spasing (g_m) in terms of all such parameters.

Figure 4.3(a) shows the behavior of g_m as Ω_a varies for different values of N_c. A drastic reduction of g_m could be observed even for much smaller values of the coherent drive, when compared with the g_m values at $\Omega_a = 0$. For a much higher number of chromophores (around 60000), it is evident that g_m gets reduced by more than a factor of 2, over more than 90% of the operating regime of Ω_a, for the spasing setup we have considered. It is also possible to observe the naturally expected reduction of g_m when the number of chromophores increases while Ω_a is kept a constant, through Fig. 4.3(a). It can also be noted that g_m reaches a minimum in each curve in Fig. 4.3(a) for Ω_a values in the vicinity of $2.5 \times 10^{12} s^{-1}$ for the N_c values considered. After this minimum, g_m illustrates a trend of increasing gradually. This follows a similar trend as $n_{21,\mathrm{th}}$ in Fig. 4.2(a). The observed growth of g_m as Ω_a reaches much higher values is due to the reduction of the positive population inversion between $|3\rangle$ and $|2\rangle$ ($n_{32,\mathrm{th}}$) as Ω_a increases, as per Eq. 4.9. Therefore, for a given number of chromophores (N_c), there exists a finite range of the coherent drive (Ω_a), such that $g_\mathrm{m} < g_{\mathrm{m},\Omega_a=0}$. Assuming $\gamma_{21} \gg \gamma_{31}, \gamma_{32}$, we derive an approximate value for the maximum of Ω_a which satisfies this condition as,

$$\Omega_{a,\max} \approx \frac{\tilde{\Omega}_b}{4} \sqrt{\frac{3 N_\mathrm{c} \gamma_{21}}{\gamma_n}}. \tag{4.22}$$

This suggests that for applications where the incoherent pumping rate is restrained to smaller values due to practical limitations, it is not possible to use arbitrarily

Table 4.1: coefficients of the simpler 4th order polynomial approximation of g_m over Ω_a for different (N_c).

$N_c(\times 10^4)$	$\mathcal{R}_4(\times 10^{-35})$	$\mathcal{R}_2(\times 10^{-11})$	$\mathcal{R}_0(\times 10^{12})$
1	4.715	1.373	5.389
2	2.835	1.022	4.818
3	2.480	0.943	4.666
4	2.331	0.908	4.595
5	2.249	0.889	4.554
6	2.197	0.876	4.527

high Ω_a values, as one might naturally expect. Equation 4.22 further suggests how to adjust this extreme limit of Ω_a through the careful use of other controllable parameters.

Apart from the detailed analysis performed using the analytical expression that can be obtained using Eq. 4.13 which we derived for g_m, we could model the main physical dependencies of the threshold requirements with simpler expressions using Taylor series expansion for the whole operating regime. After careful observation of the curves obtained in Fig. 4.3(a) it is possible to gain more physical insight into the operation of the device through such simpler expressions. We could approximate that g_m varies with Ω_a as a 4th order polynomial in the form of $\mathcal{R}_4\Omega_a^4 - \mathcal{R}_2\Omega_a^2 + \mathcal{R}_0$, where the coefficients $\mathcal{R}_4, \mathcal{R}_2$ and $\mathcal{R}_0$ depend on system specific parameters. We have tabulated the values of the coefficients for the spaser set up we have considered, for different values of N_c in Table. 4.1. These simpler approximations provide a vivid understanding of the physics behind the operation of a spaser, and they act as a valuable set of tools in design optimization as well. Figure 4.3(b) further elucidates the variation of g_m over a wide range of practical values of Ω_a and N_c. The contour plots present in Fig. 4.3(b) demonstrate equi-threshold lines for different values of g_m. Such curves present valuable guidelines on spaser design optimization.

4.3.4   The effect of decoherence

Due to environmental interactions, the spaser tends to loose the coherent super-position of its states, which yields in the destruction of spasing effect by decreasing the efficiency of energy transfer mechanisms between the plasmons and the gain medium [116, 117]. We model this phenomena by the parameter γ_{ph}, denoted as the rate of decoherence. Unlike in the previous results in Fig. 4.2 and Fig. 4.3 where γ_{ph} was taken as zero, we now consider practical non-zero values for γ_{ph} and study how it affects the spasing threshold.

According to Fig. 4.4(a), it is evident that g_m increases as γ_{ph} increases, as expected. For non-zero Ω_a values, g_m behaves approximately as a logarithmic function of γ_{ph}. It is also noticeable that for a given γ_{ph} value, g_m decreases as the coherent drive Ω_a increases, strengthening the coherence between the energy states of the system. The amount of this favourable reduction of g_m is by a factor of ~ 2 for the range of values considered in our simulations. Figure 4.4(b) demonstrates the behavior of g_m over a wide range of γ_{ph} and Ω_a using a surface plot. The dashed lines represent contour plots where g_m takes different constant values as indicated. Such curves provide guidance for the physicists to methodically optimize spaser designs to increase performance.

As per the line plots shown in Fig. 4.4(c), we could conclude that g_m exhibits a logarithmic increase as the decoherence rate (γ_{ph}) increases. This is valid for much larger values of N_c, that have been used in much of the literature [11, 31, 113]. Furthermore, it can also be noticed that, for a constant value of γ_{ph}, g_m decreases as N_c is increased. Figure 4.4(d) demonstrates the variation of g_m for a much broader range of γ_{ph} and N_c, where the dashed curves correspond to the contours where g_m is constant for a given curve.

All these numerical analyses were made possible due to the explicit analytical expressions we derived in Sec. 4.2, which could describe the spasing threshold of most general spaser setups. Therefore, it is evident that the loss of coherence

due to the interactions with the environment is properly characterized by our expressions. Our results also provide significant insights on how to mitigate the effects of decoherence in the vicinity of spasing threshold, through the optimal use of the coherent drive Ω_a and N_c.

4.4 Conclusion

In this chapter, we have studied physical parameters such as population densities, population inversions and the off diagonal coherence terms of a spaser at spasing threshold, by deriving explicit analytical expressions. We further obtained an analytical expression to describe the behavior of the minimum incoherent pumping rate required to start spasing. All these expressions comprise the many system specific parameters such as chromophore density, decay rates of the quantum emitters, plasmon decay rate, Rabi frequency of the coherent drive, rate of decoherence etc., which enables the scientists to extensively study as well as optimally fine tune the threshold characteristics depending on the application. Moreover, we obtained an expression for the minimum incoherent pumping rate required to start a two-level spaser, using the expressions we obtained for the three-level spaser setup, which reaffirms the validity of our work. We then performed a detailed numerical analysis using a silver nano-sphere based spaser to demonstrate the reduction of the incoherent pumping requirements due to the coherent drive. Here we illustrated another interesting phenomena called spasing without inversion, which is analogous to lasing without inversion in macroscopic lasers. We finally demonstrated the effect of decoherence on the threshold characteristics of the spaser to complete our study. All these results and expressions can be readily used in obtaining desired threshold characteristics for most general spaser setups for design optimization.

Chapter 5

Generalized study on spasers for design optimization

5.1 Extension to the 2-level model

We now look at how it is possible to extend the knowledge we obtained in the 3-level model to further analyze the 2-level model. The objective is to develop a comprehensive analytical framework to analytically characterize both 2-level and 3-level spasers in order for easier methods of design optimization with an extremely low computational cost.

5.1.1 Model overview

Note that we have followed the same notation as well as the formalism in the 3-level model. The same C-number approach has been utilized. Invoking the Liouville-von Neumann Master equation followed by the Heisenburg's equation of motion for the plasmon annihilation operator yields us the following complex equations, which have the same but much simpler form as the 3-level model.

$$n_{21} = \rho_{22} - \rho_{11}, \tag{5.1}$$

$$\dot{n}_{21} = -4Im(\rho_{12}a_{0n}\tilde{\Omega}_{12}) - \gamma_2(1 + n_{21}) + g(1 - n_{21}), \tag{5.2}$$

$$\dot{\rho}_{21} = -(i(\omega - \omega_{12}) + \Gamma_{12})\rho_{21} - i\tilde{\Omega}_{12}a_{0n}n_{21}, \tag{5.3}$$

$$\dot{a}_{0n} = (i(\omega - \omega_{12}) - \gamma_n)a_{0n} + iN_p\rho_{21}\tilde{\Omega}_{12}, \tag{5.4}$$

Using the same conversion from complex equations to real valued eequations, yield the following set of real-valued equations. We have used the same notation as in the 3-level model.

$$\dot{n}_{21} = -4\tilde{\Omega}_{12}(B\rho_{12,R} + A\rho_{12,I}) - \gamma_2(1 + n_{21}) + g(1 - n_{21}), \tag{5.5}$$

$$\dot{\rho}_{12,R} = -\Gamma_{12}\rho_{12,R} + \tilde{\Omega}_{12}n_{21}B,, \tag{5.6}$$

$$\dot{\rho}_{12,I} = -\Gamma_{12}\rho_{12,I} + \tilde{\Omega}_{12}n_{21}A, \tag{5.7}$$

$$\dot{A} = -(\omega - \omega_n)B - \gamma_n A + N_p\rho_{12,I}\tilde{\Omega}_{12}, \tag{5.8}$$

$$\dot{B} = (\omega - \omega_n)A - \gamma_n B + N_p\rho_{12,R}\tilde{\Omega}_{12}, \tag{5.9}$$

$\omega - \omega_n$ is defined as the detuning (Δ_n) between the spasing transition and the SP mode. Performing numerous indicative numerical simulations for the scenarios given in [11], where $\gamma_{ph} = 15.2 \times 10^{12}s^{-1}$, we conclude that in order to make the coupled differential equations which describe the spasing action of a 2-level spaser at steady state, we need to make $\Delta_n = 0$ where the original values was $\Delta_n = 3 \times 10^{12}s^{-1}$. This is by following the same approach we utilized in solving the 3-level model in chapter 3. Therefore, if the same method can be utilized to derive an analytical equation to describe the spasing power of a 2-level spaser accurately, we can then conclude that it is possible to use our method to solve such sets of coupled differential equations which describe active plasmonic nano-structures. The following set of equations can be obtained by making all time derivatives equal to zero at steady state.

$$0 = -4\tilde{\Omega}_{12}(B\rho_{12,R} + A\rho_{12,I}) - \gamma_2(1 + n_{21}) + g(1 - n_{21}), \tag{5.10}$$

$$0 = -\Gamma_{12}\rho_{12,R} + \tilde{\Omega}_{12}n_{21}B, \tag{5.11}$$

$$0 = -\Gamma_{12}\rho_{12,I} + \tilde{\Omega}_{12}n_{21}A, \tag{5.12}$$

$$0 = -(\omega - \omega_n)B - \gamma_n A + N_p\rho_{12,I}\tilde{\Omega}_{12}, \tag{5.13}$$

$$0 = (\omega - \omega_n)A - \gamma_n B + N_p\rho_{12,R}\tilde{\Omega}_{12}, \tag{5.14}$$

By solving the above set of algebraic equations yields the following simple expression for the number of SPs generated per spasing mode (N_n) for a 2-level spaser.

$$N_n = \frac{1}{4}\left[\frac{N_p}{\gamma_n}(g - \gamma_2) - \frac{\Gamma_{12}}{\tilde{\Omega}_{12}^2}(g + \gamma_2)\right] \tag{5.15}$$

Mapping the parameters from the 3-level model to the 2-level model to maintain consistency, we arrive at our final equation to describe the spasing power as follows:

$$N_n = \frac{1}{4}\left[\frac{N_p}{\gamma_n}(g - \gamma_{21}) - \frac{\gamma_{ph}}{\tilde{\Omega}_{12}^2}(g + \gamma_{21})\right] \tag{5.16}$$

5.1.2   Physical insights

In order to study the dependency of N_n versus the incoherent pumping rate (g), we re-arrange the equation for N_n as follows:

$$N_n = \frac{1}{4}\left[g(\frac{N_p}{\gamma_n} - \frac{\gamma_{ph}}{\tilde{\Omega}_{12}^2}) - \gamma_{21}(\frac{N_p}{\gamma_n} + \frac{\gamma_{ph}}{\tilde{\Omega}_{12}^2})\right] \tag{5.17}$$

Eq. 5.17 represents the equation of a straight line, and it resembles a similar dependency as it is shown in the numerical simulations done in [11, 18]. Furthermore, it is also possible to derive 5.17 from 5.19 by setting $\Omega_a = 0$, $\gamma_{31} = 0$ and $\gamma_{32} >> \gamma_{21}$. When the above parameters are set, eq. 5.19 provides a similar result to that of 5.17.

5.2 Coherence enhanced graphene spaser

5.2.1 Overview
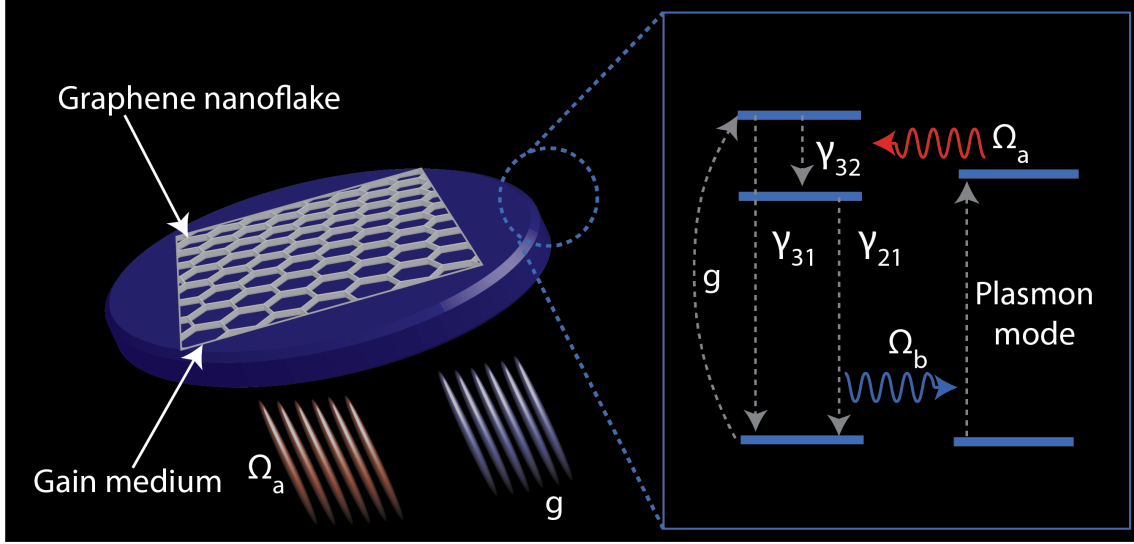
Figure 5.1: Structure and the energy flow diagram of the proposed SPASER: Gain medium chromophores are excited via incoherent pumping (g) as well as a coherent drive Ω_a. The spasing transition $|2\rangle \rightarrow |1\rangle$ is coupled to one of the SP modes in the graphene nanoflake. Decay rates of the corresponding energy levels are denoted by γ_{21}, γ_{32} and γ_{31}. The Rabi frequency for the coupling between the spasing transition and the SP mode is denoted by Ω_b.

Due to the many advantages such as thermal and chemical stability, mechanical strength and bio-compatibility, graphene has been proposed as a potential plasmonic resonator for spasers [55]. On the other hand, to address weaknesses present in conventional 2-level gain medium based spasers, gain medium chromophores have been modelled as 3-level systems recently [31,113]. Furthermore, it became monumental for the spaser technology when the first experimental realization of a 3-level spaser came to fruition in 2018 by Song *et al.* [27].

Therefore, in this section, we present the first spaser design which couples 3-level gain chromophores with a graphene plasmonic resonator. Enhanced output power, increased immunity for decoherence, lowering of the spasing threshold

and more flexibility in design optimization could be observed in the results.

5.2.2 Graphene as a plasmonic material

Ever since the fabrication of new allotropes such as graphene, carbon nano-tubes and fullerenes [118], carbon has revolutionized the metamaterials research [119]. Due to its remarkable properties such as higher electrical conductivity [120], mechanical strength [121] and thermal stability [122], graphene has specifically gained much attention. One the other hand, due to its two-dimensional nature and the honey comb lattice structure, it has also been reported that graphene supports SP excitations with better confinement and low dissipation, compared to SPs generated on noble metal surfaces. The other most noteworthy feature of graphene is that its optical properties can be tuned using doping [123]. Therefore, graphene has become a promising contender for plasmonic resonators in spasers.

The permittivity of graphene can be expressed as

$$\epsilon(\omega) = 1 + \frac{\sigma(\omega)}{\epsilon_0 \omega}, \tag{5.18}$$

where $\sigma(\omega)$ is the optical conductivity at angular frequency ω. $\sigma(\omega)$ can be expressed as $\sigma_{intra}(\omega) + \sigma_{inter}(\omega)$, where $\sigma_{intra}(\omega)$ and $\sigma_{inter}(\omega)$ are the intra band and inter band conductivities of graphene, respectively. ϵ_0 is the conductivity of free space.

5.2.3 Model description

Figure 5.1 presents a pictorial illustration of the proposed spaser model. We adopt the standard semi classical theory along with a density matrix formalism to describe spasing action, which is similar to the approach presented in chapter 3. Furthermore, it has been modelled as an open quantum system, in order to ac-

count for decaying and dephasing (decoherence). [113].

The quantum emitters are placed homogeneously. Shahbazyan *et al.* [107] has proved that this is possible for different mode volumes. Most of the edge effects (i.e. zigzag, armchair, chiral) of the graphene nano-flake on the distribution of emitters can be addressed using this method. We also make sure that the dimensions of the graphene nano-flake stay in the limits specified in [124], so that the conductivity models are accurate enough to neglect the edge effects. Furthermore, same as the previous sections, we assume that the quantum emitters interact with the plasmon mode uniformly. These assumptions are necessary to generate the insights from our analytical method. It provides a back-of-the-envelope approach to simply analyse the main output behaviors of the device.

5.3   Results and Discussion

We have derived an exact analytical expression to describe the number of SPs per spasing mode (N_n), which describes the output power of the spaser by taking into account both inputs (g and Ω_a) as well as all system specific parameters.

$$
N_n = \Big[(-8\gamma_n \mathcal{F}_5((\Gamma_{21}\Gamma_{31}\gamma_n + \gamma_n\Omega_a^2)\mathcal{F}_{10} \\
+ N_c\tilde{\Omega}_b^2(\Gamma_{31}\Gamma_{32}\mathcal{F}_4 + \Omega_a^2\mathcal{F}_7)) + \mathcal{F}_8^2)^{\frac{1}{2}} - \mathcal{F}_8 \Big] \frac{1}{\mathcal{F}_9},
$$

(5.19)

where $\mathcal{F}_1 = \Gamma_{32}(2\gamma_{31} + 2\gamma_{32} + g) + 6\Omega_a^2$, $\mathcal{F}_2 = \gamma_{21}(\gamma_{31} + \gamma_{32} + g) + \gamma_{32}g$, $\mathcal{F}_3 = \gamma_{21} - 3\gamma_{31} - \gamma_{32} - 3g$, $\mathcal{F}_4 = \gamma_{21}\gamma_{31} + \gamma_{21}\gamma_{32} - \gamma_{32}g$, $\mathcal{F}_5 = 2\gamma_{31} + 2\gamma_{32} + g$, $\mathcal{F}_6 = \gamma_{21} + \gamma_{31} + 2g$, $\mathcal{F}_7 = 2\gamma_{31}\Gamma_{31} - 2\Gamma_{31}g + 2\Gamma_{31}\gamma_{21} - \gamma_{21}g$, $\mathcal{F}_8 = 2\gamma_n\Gamma_{31}\mathcal{F}_1 + \gamma_n\Gamma_{21}\mathcal{F}_2 + 2\gamma_n\Omega_a^2\mathcal{F}_3 + N_c\tilde{\Omega}_b^2\mathcal{F}_4$, $\mathcal{F}_9 = 4\gamma_n\mathcal{F}_5\tilde{\Omega}_b^2$ and $\mathcal{F}_{10} = \Gamma_{32}\mathcal{F}_2 + 2\Omega_a^2\mathcal{F}_6$ [113]. Γ_{21}, Γ_{32} and Γ_{31} are the relaxation rates of the corresponding energy levels of the chromophores. The parameters γ_n, N_c and $\tilde{\Omega}_b$ are the plasmon decay rate, number of gain chromophores and single plasmon Rabi frequency, respectively. For

the purpose of simulation, plasmon resonance frequency of graphene is taken as 1.55 eV with a Fermi energy of 0.956 eV and plasmon decay rate of 0.0128 eV [125, 126]. Figure 5.2 (a) clearly suggests that the proper use of Ω_a can significantly enhance the power output ($\propto N_n$) of graphene based spasers. Furthermore, it is evident from Fig. 5.2 (b) that the negative effects of decoherence(γ_{ph}) on graphene spaser output can be overcome by the use of Ω_a. In addition, Fig. 5.2 (c) illustrates the possibility of using Ω_a to achieve the same output power with the use of smaller chromophore densities (ρ). These results provide significant insights on the operation of spasers, and it is possible to derive many simpler analytical approximations for the curves given in Fig. 5.2 by limiting the physical parameters within the practically used regimes. Even though we have illustrated a particular spaser set up in this section, it is possible to utilize our scheme to carefully tailor graphene related parameters such as plasmon resonance frequency, plasmon decay rate, Fermi energy, dimensions etc., to optimally achieve a wide range of spasing output power requirements.

Whilst the proposed model provides a general framework to design graphene based 3-level spasers, it can be used to compare the performance of the 3-level model and the 2-level model. The $\Omega_a = 0$ curves in fig. 5.2 gives an approximate idea on the performance of a generic 2-level model where the only form of input is the incoherent pumping source, g. For example, a significant output power enhancement has been achieved in the three-level model, where N_n shows an approximate 3-fold increase when $\Omega_a = 2 \times 10^{12} s^{-1}$ compared with the corresponding 2-level scenario. It can be observed that the threshold pumping requirement stays approximately around the same value. Similar observations can be made to compare the performance of our model and the conventional 2-level structure by changing chromophore density (ρ) and decoherence rate (γ) as well, using fig. 5.2.
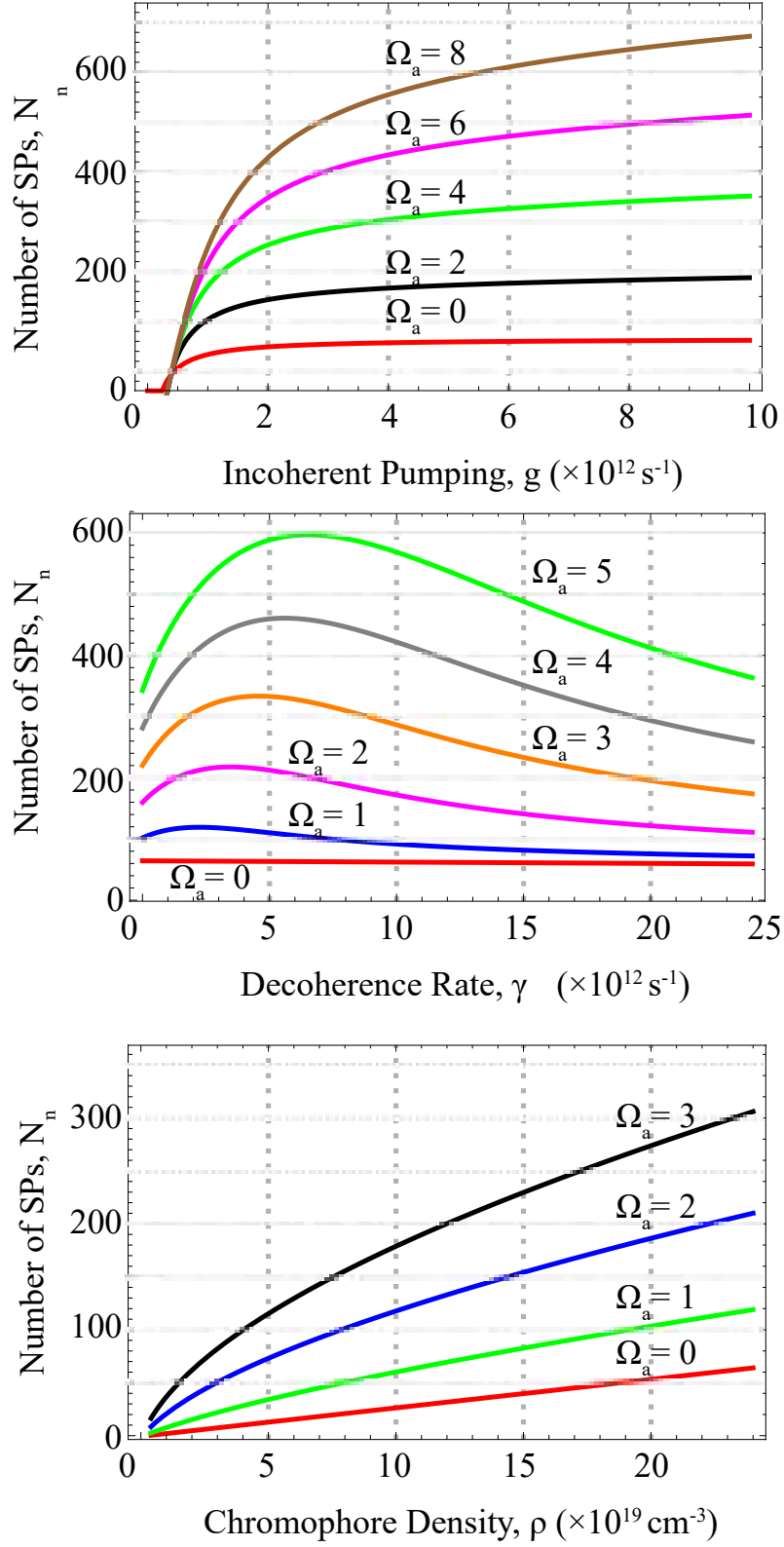
Figure 5.2: Subfigures (a)-(c) illustrate the behavior of N_n against g, γ_{ph} and ρ respectively for different values of the coherent drive, Ω_a. All illustrated values of Ω_a are given in units of $10^{12}\,\mathrm{s}^{-1}$.

5.3.1 Conclusion

We have coupled a graphene nanoflake with a 3-level gain medium and have powered it using the usual incoherent drive as well as an additional coherent field to achieve better performance characteristics in spasers. Our work provides guidelines for design optimization as well as for better understanding the physics of realizing robust and efficient sources of SPs for nano-technological and biomedical applications.

This page intentionally left blank.

Chapter 6

Effects of external plasmonic fields on 3-level spasers

In this chapter, as the final objective of the thesis, we study the effects of external plasmonic feedback for the operation of a 3-level spaser. In practice, we would not be dealing with a single spaser isolated from external plasmonic fields. Instead, networked systems of interacting spasers will be utilized in different applications. Therefore, it is essential that we study the interaction dynamics of spasers. We have extended the already established knowledge in this thesis to accomplish this objective using a simple yet effective manipulation of system configuration. The effect of external plasmonic fields on the operation of a single spaser will be studied in this chapter. It formulates a framework to study the interactions of two or more spasers in complex circuits.

6.1   Model Overview

We explore how two coherently enhanced 3-level spasers interact with each other. Several studies have been performed to explore the interaction between conventional spasers [127,128]. Due to their many promising properties that we have illustrated throughout this thesis, interaction between coherence enhanced 3-level spasers needs to be investigated.

The schematic diagram of the system is depicted in fig. 6.1, where all relevant

physical parameters are illustrated. The main difference between a single coher-
ence enhanced 3-level spaser and the system under consideration is that there is
a term to describe the interaction between the spasers. We denote it by Ω_{NP-NP},
the interaction Rabi frequency [129]. The basic mathematical model governing
the behavior of a single spaser is the same as presented in chapter 3. We denote
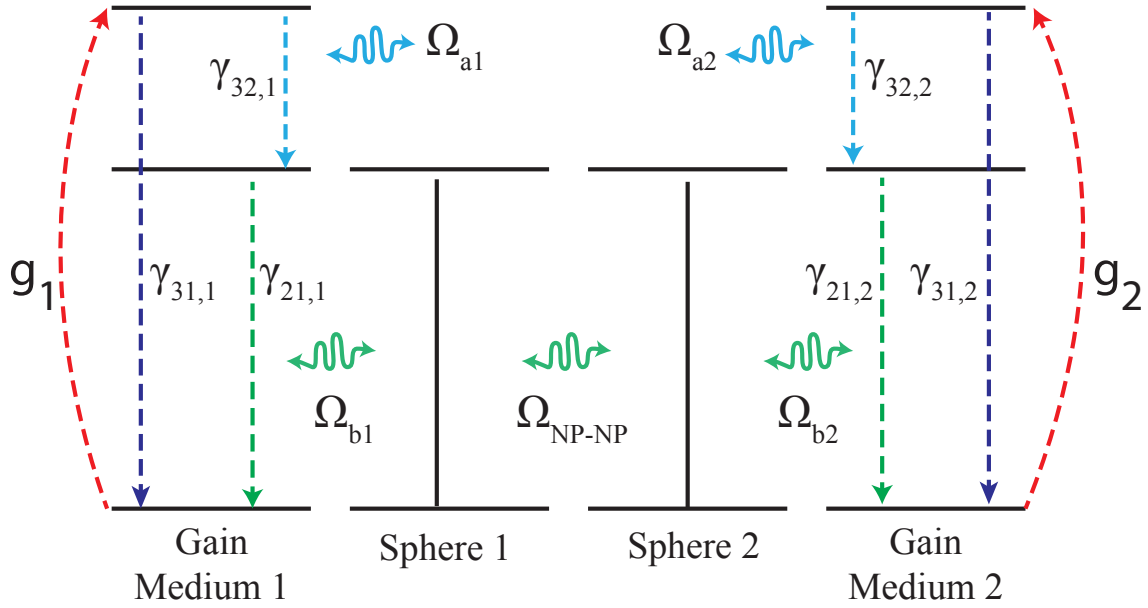
Figure 6.1: Basic energy flow diagram of two interacting spasers. We ideally
assume that the two spasers are controlled using different coherent drives (Ω_{a1},
Ω_{a2}) and incoherent pumps (g_1, g_2). All other decay terms and interaction terms
are similar to what was presented in fig. 3.1. The main difference is the interaction
Rabi frequency (Ω_{NP-NP})

the effective plasmonic field experienced by spaser 1 by the corresponding Rabi
frequency as $\Omega_{b1}^{eff}(t)$. It can be expressed as:

$$\Omega_{b1}^{eff}(t) = \Omega_{b1}(t) + \Omega_{NP-NP}(t) \tag{6.1}$$

We model $\Omega_{NP-NP}(t)$ as $c_f \Omega_{b1}(t - \tau_f) + c_p \Omega_{b2}(t - \tau_p)$, where c_f is the feedback
strength (from back-scattered plasmonic field from spaser 1) and c_p is the attenu-
ation factor of the plasmonic field from spaser 2. τ_f and τ_p are the corresposding

time delays. Therefore, the effective plasmonic field experienced by a spaser can be expressed as:

$$\Omega_{b1}^{eff}(t) = \Omega_{b1}(t) + c_f \Omega_{b1}(t - \tau_f) + c_p \Omega_{b2}(t - \tau_p). \tag{6.2}$$

6.2 Numerical Simulations

Two identical silver nano-spheres of radius 40 nm are used as the plasmonic nano-structure. All values of parameters are taken similar to what we used in chapters 3 and 4, where the plasmon resonance frequency (ω_n) and the plasmon decay rate (γ_n) are as $2.5eV$ and $5.3 \times 10^{14} s^{-1}$ respectively. As the two gain mediums, two sets of generic quantum emitters are used with decay rates, $\gamma_{21} = 4 \times 10^{12} s^{-1}$, $\gamma_{32} = 4 \times 10^{11} s^{-1}$ and $\gamma_{31} = 4 \times 10^{10} s^{-1}$. The relative permittivity of the submerging dielectric medium is taken as $\epsilon_d = 2.25$, as in [31]. The bulk permittivity values of silver are obtained from the Johnson and Christy model [70]. For the simplicity of analysis, we assume that both spasers are given identical inputs, i.e. $\Omega_{a1} = \Omega_{a2}$ and $g_1 = g_2$.

We first study the time evolution of the output power in one of the spasers. Since we assume that both spasers are identical and they are powered by identical inputs, studying the dynamics of one spaser is sufficient for a complete understanding. Since the output power is indicated by N_n [110], we simulate N_n under 4 different scenarios to understand the physics of these interactions, as described in fig. 6.2. We set $\Omega_a = 4 \times 10^{12} s^{-1}$ and $g_1 = g_2 = 16 \times 10^{12} s^{-1}$. From fig. 6.2, it is evident that after the initial transients, N_n reaches steady state, generating a constant output power in all four scenarios. The times at which they reach steady state vary with the properties of the external plasmonic feedback. This occurs mainly due to τ_p and τ_f, the delay times it takes for the external plasmonic feedback and the back scattering to take effect on the considered spaser. For example,
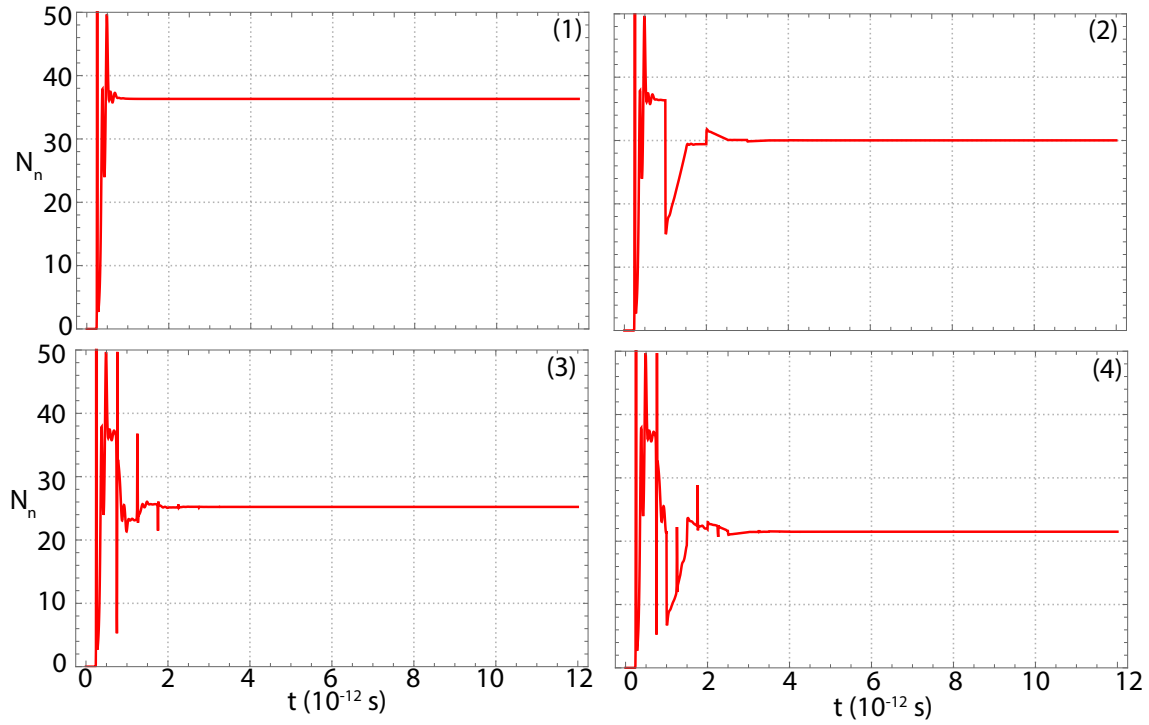
Figure 6.2: Time evolution of the output power (N_n) of a spaser which is interacting with another spaser. We have presented 4 possible scenarios in the 4 graphs as labelled. Scenario (1): $c_f = 0$ and $c_p = 0$, which is effectively a single spaser operating without the effect of any external plasmonic fields. Scenario (2): $c_f = 0.1$ and $c_p = 0$, this is where there is only back-scattering. Scenario (3): $c_f = 0$ and $c_p = 0.2$ where there is no back-scattered plasmonic field, but there is direct plasmonic field from the other spaser. Scenario (4): $c_f = 0.1$ and $c_p = 0.2$

in scenario (1), according to fig. 6.2 (1), where there is no such external plasmonic effects, the spaser reaches the steady state quicker. Furthermore, for the same set of inputs and system configurations, the value of N_n changes in each scenario due to the different feedback strengths (c_p) and attenuation factors (c_f).

6.3 Steady state behavior

In order to investigate this we generate the spasing curves for each scenario to further investigate this phenomena at steady state. The results are illustrated in fig. 6.3. According to fig. 6.3, we can observe that the plasmonic feedback as well
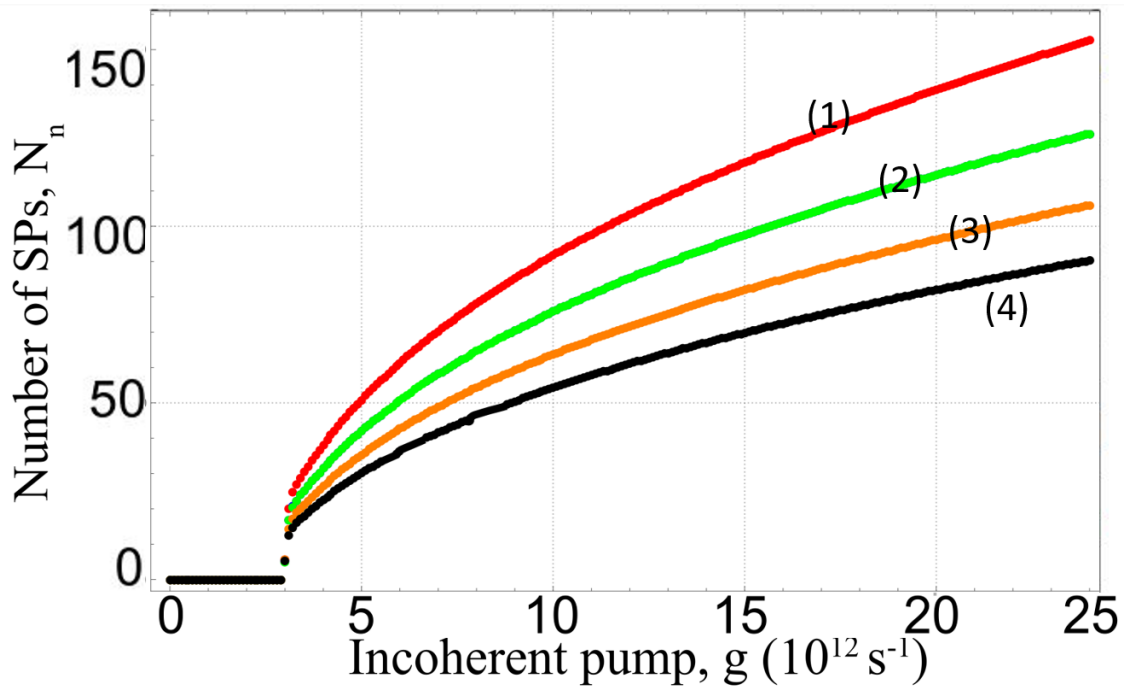
Figure 6.3: Steady state output power (N_n) of a spaser which is interacting with another spaser. We have presented 4 possible scenarios in the graph as labelled. Scenario (1): $c_f = 0$ and $c_p = 0$, which is effectively a single spaser operating without the effect of any external plasmonic fields. Scenario (2): $c_f = 0.1$ and $c_p = 0$, this is where there is only back-scattering. Scenario (3): $c_f = 0$ and $c_p = 0.2$ where there is no back-scattered plasmonic field, but there is direct plasmonic field from the other spaser. Scenario (4): $c_f = 0.1$ and $c_p = 0.2$

as external plasmonic fields certainly have an impact on the output characteristics of coherence enhanced spasers. To analyse this further, we take the effective Rabi frequency we defined in eq. 6.2. In general, $\Omega_{b1}^{eff}(t)$ is a function of time. However, through the observations in fig. 6.2, it is clear that N_n becomes a constant after a sufficient amount of time. This indicates that $\Omega_{b1}^{eff}(t)$ should also become a constant at the steady state operation. Therefore, at steady state, we can write

$$\Omega_{b1}^{eff}(T) = \Omega_{b1}(T) + c_f \Omega_{b1}(T) + c_p \Omega_{b2}(T), \qquad (6.3)$$

for a large enough T. Furthermore, since we assume that both spasers are identical, $\Omega_{b1} = \Omega_{b2}$. As a result, eq. 6.3 can be further simplified as

$$\Omega_{b1}^{eff} = (1 + c_f + c_p)\Omega_{b1} \qquad (6.4)$$

According to the definition in chapter 3, $\Omega_{b1} = k\tilde{\Omega}_b$. Therefore, by substituting eq. 6.4 in 5.19, we can perform a quite accurate back-of-the-envelope analysis on N_n analytically, without numerically solving for the whole system.

This can be used to explain the difference of N_n from scenario (1) to (4), as depicted in fig. 6.3. Once we move along scenarios, from (1) to (4), the c_f and c_p values change. As a result, according to eq.6.4, the effective single plasmon rabi frequency (Ω_{b1}^{eff}) has the largest value in scenario (4) among the 4 cases considered, and scenario (1) has the lowest. Substituting these values in our analytical characterization in eq. 5.19 explains the difference of output in the 4 scenarios considered. Therefore, the effective single plasmon rabi frequency (Ω_{b1}^{eff}) is the key parameter that governs the output power during this interaction according to the proposed model.

In addition, using the already established knowledge in this thesis, it can be concluded that the coherent drive Ω_a can be utilized to change the output of the 3-level spaser, under the effect of external plasmonic fields.

6.4 Conclusion

We have developed a simple, yet effective framework for analysing the inter-
actions between two coherently enhanced spasers. Under certain assumptions,
we have also demonstrated that it is possible to characterize the output of such
spasers analytically, generating a lot of physical insights for design optimiza-
tion. The values of c_f and c_p depend on the waveguide connecting the spasers
[130, 131] and the dielectric material they are contained in [132]. Therefore, by
carefully selecting the waveguides and the dielectric, it is possible to tune c_f and
c_p to adjust the output of the interacting spasers, using our approach.

This page intentionally left blank.

Chapter 7
Contributions and future work

This chapter summarises the contributions made to the advancement of scientific literature through the work presented in this thesis, followed by suggestions for future work.

7.1 Significance of Contributions

Complete analytical characterization of the output power of a 3-level spaser

We derived approximate analytical expressions to characterize the spasing (L-L) curve of a coherently enhanced spaser with 3-level gain-medium chromophores in chapter 3. Owing to the compact nature of the analytical expressions, our solution also facilitates the grouping and identification of key processes responsible for spasing action, whilst providing significant physical insights. Furthermore, we illustrated that our expression generates results within 0.1% error compared to numerically obtained results for pumping rates within the operating regime.

An analytical approximation drastically reduces the computational power required to calculate the spaser output by several orders of magnitude, compared to the numerical simulations. One may argue that during the current era of super-computers that can process up to several peta-flops of information, reduction of computational cost is insignificant. However, given the fact that scientists are currently modelling only single spasers or a very few number of spasers at most,

when the technology of nanoplasmonics grows into widespread use, several millions of such devices might have to be interconnected and modelled. In such scenarios, computational cost may become extremely vital.

These results have been communicated in *Applied Physics Letters* [113].

A novel approach to solve systems of coupled, non-linear partial differential equations

In chapters 3 and 4, we have provided a novel method to transform a set of coupled differential equations into a set of coupled algebraic equations, which enables such a system of equations to be solved analytically. This method overpowers even the most state-of-the-art partial differential equation solvers found in Matlab and Mathematica, when the systems under consideration are resonantly or near resonantly coupled. This has been illustrated in both chapter 3 and 5, where we solve for both 2-level and 3-level spaser configurations. This unique approach incorporates considerable engineering intuition and physical insight. We have proven that the effect of the assumption is negligible by illustrating that the error between the numerical and analytical solutions is less than 0.1% for the whole operating regime. Such an approach will enable systems of the same type to be solved analytically to a very high accuracy.

Analytically characterizing the output power of a 2-level spaser

So far in literature, the output of the conventional 2-level spasers has also been obtained numerically. Using the method we developed in chapter 3, we obtained such simpler analytical expressions to describe the output characteristics of a 2-level spaser. It provides the scientific community with the same set of benefits it provided for 3-level spasers such as simpler yet effective physical insights, design optimization capabilities and computational cost reductions.

Characterization of physical properties at spasing threshold

We have derived explicit analytical expressions for population inversions, population densities as well as non-zero off-diagonal terms of the density matrix at spasing threshold. Moreover, we have analytically studied the minimum incoherent pumping rate required to start spasing. The derived expressions comprise all system specific parameters, enabling one to gauge how the threshold condition changes with different values of parameters. It further facilitates design optimization of spasers at lower pumping energies as well. We have also obtained simpler approximate expressions, providing better physical insights into the operation of the device. Furthermore, a detailed numerical analysis was performed, quantifying the reduction of minimum pumping requirements at spasing threshold due to the coherent drive, whilst demonstrating the phenomena of spasing without inversion. Finally, we have scrutinized the effects of decoherence on the spasing threshold to complete the analysis. These generalized results and expressions can be applied to most spaser setups to study and optimize their respective threshold characteristics.

These results have been drafted to be communicated in *Journal of Physics: Condensed Matter*

Forming the basis for design optimization of spasers

We enable optimization of the large parameter space associated with spaser designing, a functionality not offered by the methods currently available in literature. This is vital for the advancement of spaser technology towards the level of device realization. In a numerical approach, even though it is possible to calculate the output by setting the known inputs and system configuration, it is not easy to solve for, fine tune and optimize the required inputs and system configurations to generate a desired output. The crucial role played by simple analytical models

(e.g. laser L-I curves) in the evolution of semiconductor laser technology is well renowned. It is natural to assume that various applications in nano-plasmonics demand such intuitive design models as well. The only way to achieve such design flexibility is by means of explicit analytical expressions. We believe that the analytical solution we have derived would cater to this crucial requirement.

An analytical characterization helps to understand the underlying physics behind the operation of a spaser. After deriving an explicit analytical expression, we have investigated and presented the main dependencies of the spaser output on the two different inputs, incoherent pumping rate (g) and the coherent drive (Ω_a) respectively, over the whole operating regime. The main dependency of N_n on all other variables can also be derived using our explicit analytical expressions in Chapter 3 and Chapter 4. Such simple models would be quite beneficial to study the general behavior of the spaser output. These new knowledge would cater as the basis for spaser design optimization.

These results have also been included in our journal article published in *Applied Physics Letters* [113].

First implementation of a 3-level spaser based on graphene

Due to various desirable physical properties such as chemical stability, mechanical strength and bio compatibility, graphene has emerged as a potential plasmonic material. We also have proved that the 3-level model over powers the 2 level model in many aspects. Therefore, in chapter 5 we combined the best of both worlds by designing and implementing the first 3-level spaser based on graphene, where we used a 2 dimensional graphene nano flake as the plasmonic resonator. We further illustrated that it shows improved output characteristics compared to its 2-level counterpart. These results have been communicated in *Advanced Photonics Congress* organized by OSA (*Optical Society of America*) in 2019 [133].

Theoretical framework to study the effects of external plasmonic fields

In practice, spasers will not be operated as isolated devices, but as parts of complex plasmonic circuits. Therefore, in chapter 6, we established a simple, yet effective theoretical framework to study the interaction of 3-level spasers. It takes into account both the external plasmonic fields as well as the own plasmonic field which gets reflected, when modelling the behavior of a 3-level spaser under external plasmonic fields. Furthermore, we proved that back-of-the-envelope calculations can be performed on the output behavior of such spasers, using the expressions we have derived. This will pave way for the utility of spasers in many applications, while providing simple and intuitive knowledge on spaser design optimization as well.

7.2 Suggestions for future work

The work entailed in this thesis can be extended in many experimental and theoretical pathways. We have outlined a few such directions as follows.

Analyze the stability of spasers

Throughout our work, resonant coupling was assumed in all the energy transfer processes which govern the spaser operation. Therefore, all the detunings were assumed to be zero. Yet, for a practical realization of a spaser, it is essential that we perform an in depth stability analysis to define the limits of detunings within which the spaser can safely operate. In that regard, an improved set of expressions can be derived by releasing the assumption of resonant coupling to analyze the stability of the 3-level spaser. With that in mind, laser, which is the macro-scale counter part of the spaser, could also be investigated to map the concepts such as Lyapunov stability [134], pump induced relative intensity noise [135] and

injection locking [136] since both the devices are closely related in structure and operation.

Study the response of spasers to modulated inputs

Throughout our thesis, we have studied the Continuous Wave (CW) operation of the spaser in the steady state regime, with performance enhancement as the basic point of interest. For a broader understanding of the spaser behavior, dynamic characteristics of the device should also be investigated. On that account, modulation response and pulse response can be studied by varying the frequency and amplitude of the coherent drive. In addition, the potential of providing the incoherent pumping as pulses to power the spaser may also be studied. Integrating such modulation and pulse operation techniques together to generate practically usable forms of output pulses from the 3-level spaser will be of great interest [137]. It will strengthen the potential of the spaser to be utilized in a lot of applications such as sensing, imaging, bio-optics etc [89, 138].

Spasers with non-homogeneous gain medium

Throughout our work thus far, we have assumed that the quantum emitters (chromophores) in the gain medium are identical, hence they interact with the plasmon mode as well as the external inputs identically. However, when realizing spasers experimentally, we may have to consider impurities such as differences in band gaps and variation of coupling coefficients in the emitters. Modelling such imperfections will be a challenge, and it will definitely enhance the modelling accuracy of spasers.

Design and analyse 3-level spasers made of different plasmonic materials

Other than noble metals and graphene, which we have studied in this thesis, many promising materials have been used in conventional 2-level spasers as the plasmonic resonator. Some examples are Molybdenum Disulfide [83, 139], black phosphorus [140] and aluminium [141, 142]. The ability to coherently enhance the output characteristics of spasers made of such materials can be explored, to enhance the spectrum of possible applications.

Formulation of a fully quantum mechanical analysis for coherence enhanced spasers

We started our analysis using quantum mechanical operators to describe the physical quantities but for the simplicity of analysis, we adopted to standard semi-classical theory when solving the system. A fully quantum mechanical solution may provide more insights into the operation of the device. This is a completely abstract area of significant potential towards the advancement of nano-plasmonics in general. As the high performance parallel computational facilities get more advanced, such a model can provide a lot more accuracy in the theoretical work. Consequently, such a model can enhance the practical realization of many active plasmonic devices.

Modelling the heating effects of coherence enhanced spasers

Thermal stability and performance variation of spasers at different operating temperatures have not been studied much. The main channels of heat generation of a spaser are metal absorption at pumping and spasing wave-lengths and non-radiative relaxations in the gain material. Most applications in bio-medicine and cancer therapy requires spasers to work in high temperature environments. Therefore, the operation of spasers leads to a temperature rise in the spaser itself,

which might damage the device. However, very little experimental or theoretical/modeling work in this area is available at present. None of the current models of spasers consider temperature as an explicit variable of interest in modeling. Therefore, it will be a significant contribution for the practical realizability and application of spasers, if temperature effects can be modelled accurately.

Bibliography

[1] Lim, A. E.-J. *et al.* Review of silicon photonics foundry efforts. *IEEE Journal of Selected Topics in Quantum Electronics* **20**, 405–416 (2013).

[2] Prasad, P. N. *Nanophotonics* (John Wiley & Sons, 2004).

[3] Premaratne, M. & Agrawal, G. P. *Light propagation in gain media: optical amplifiers* (Cambridge University Press, 2011).

[4] Ringe, E. *et al.* Unraveling the effects of size, composition, and substrate on the localized surface plasmon resonance frequencies of gold and silver nanocubes: a systematic single-particle approach. *The Journal of Physical Chemistry C* **114**, 12511–12516 (2010).

[5] Ozbay, E. Plasmonics: merging photonics and electronics at nanoscale dimensions. *science* **311**, 189–193 (2006).

[6] Li, M. *et al.* Harnessing optical forces in integrated photonic circuits. *Nature* **456**, 480–484 (2008).

[7] Gettapola, K., Hapuarachchi, H., Stockman, M. I. & Premaratne, M. Control of quantum emitter-plasmon strong coupling and energy transport with external electrostatic fields. *Journal of Physics: Condensed Matter* **32**, 125301 (2019).

[8] Maier, S. A. *et al.* Plasmonics—a route to nanoscale optical devices. *Advanced materials* **13**, 1501–1505 (2001).

[9] Maier, S. A. *et al.* Local detection of electromagnetic energy transport below the diffraction limit in metal nanoparticle plasmon waveguides. *Nature materials* **2**, 229–232 (2003).

[10] Premaratne, M. & Stockman, M. I. Theory and technology of spasers. *Advances in Optics and Photonics* **9**, 79–128 (2017).

[11] Stockman, M. I. The spaser as a nanoscale quantum generator and ultrafast amplifier. *Journal of Optics* **12**, 024004 (2010).

[12] Barnes, W. L., Dereux, A. & Ebbesen, T. W. Surface plasmon subwavelength optics. *nature* **424**, 824–830 (2003).

[13] Bloemer, M. J., Buncick, M., Warmack, R. & Ferrell, T. Surface electromagnetic modes in prolate spheroids of gold, aluminum, and copper. *JOSA B* **5**, 2552–2559 (1988).

[14] Klimov, V. *et al.* Optical gain and stimulated emission in nanocrystal quantum dots. *science* **290**, 314–317 (2000).

[15] Norris, D. J., Sacra, A., Murray, C. & Bawendi, M. Measurement of the size dependent hole spectrum in cdse quantum dots. *Physical review letters* **72**, 2612 (1994).

[16] Michalet, X. *et al.* Quantum dots for live cells, in vivo imaging, and diagnostics. *science* **307**, 538–544 (2005).

[17] Gamacharige, D. L., Gunapala, S. D., Stockman, M. I. & Premaratne, M. Significance of the nonlocal optical response of metal nanoparticles in describing the operation of plasmonic lasers. *Physical Review B* **99**, 115405 (2019).

[18] Stockman, M. I. Nanoplasmonics: past, present, and glimpse into future. *Optics express* **19**, 22029–22106 (2011).

[19] Bergman, D. J. & Stockman, M. I. Surface plasmon amplification by stimulated emission of radiation: quantum generation of coherent surface plasmons in nanosystems. *Physical review letters* **90**, 027402 (2003).

[20] Abeywickrama, C., Premaratne, M., Gunapala, S. D. & Andrews, D. L. Impact of a charged neighboring particle on förster resonance energy transfer (fret). *Journal of Physics: Condensed Matter* **32**, 095305 (2019).

[21] Weeraddana, D., Premaratne, M. & Andrews, D. L. Direct and third-body mediated resonance energy transfer in dimensionally constrained nanostructures. *Physical Review B* **92**, 035128 (2015).

[22] Lisyansky, A., Nechepurenko, I., Dorofeenko, A., Vinogradov, A. & Pukhov, A. Channel spaser: Coherent excitation of one-dimensional plasmons from quantum dots located along a linear channel. *Physical Review B* **84**, 153409 (2011).

[23] Chang, S.-W., Ni, C.-Y. A. & Chuang, S. L. Theory for bowtie plasmonic nanolasers. *Optics express* **16**, 10580–10595 (2008).

[24] Fabian, J., Nakazumi, H. & Matsuoka, M. Near-infrared absorbing dyes. *Chemical Reviews* **92**, 1197–1226 (1992).

[25] Oulton, R. F. *et al.* Plasmon lasers at deep subwavelength scale. *Nature* **461**, 629–632 (2009).

[26] Plum, E., Fedotov, V., Kuo, P., Tsai, D. & Zheludev, N. Towards the lasing spaser: controlling metamaterial optical response with semiconductor quantum dots. *Optics express* **17**, 8548–8551 (2009).

[27] Song, P. *et al.* Three-level spaser for next-generation luminescent nanoprobe. *Science advances* **4**, eaat0292 (2018).

[28] Warnakula, T., Gunapala, S. D., Stockman, M. I. & Premaratne, M. Cavity quantum electrodynamic analysis of spasing in nanospherical dimers. *Physical Review B* **100**, 085439 (2019).

[29] Warnakula, T., Stockman, M. I. & Premaratne, M. Improved scheme for modeling a spaser made of identical gain elements. *JOSA B* **35**, 1397–1407 (2018).

[30] Noginov, M. *et al.* Demonstration of a spaser-based nanolaser. *Nature* **460**, 1110–1112 (2009).

[31] Dorfman, K. E. *et al.* Quantum-coherence-enhanced surface plasmon amplification by stimulated emission of radiation. *Physical review letters* **111**, 043601 (2013).

[32] Zayats, A. V., Smolyaninov, I. I. & Maradudin, A. A. Nano-optics of surface plasmon polaritons. *Physics reports* **408**, 131–314 (2005).

[33] Hutter, E. & Fendler, J. H. Exploitation of localized surface plasmon resonance. *Advanced materials* **16**, 1685–1706 (2004).

[34] Maier, S. A. *Plasmonics: fundamentals and applications* (Springer Science & Business Media, 2007).

[35] Willets, K. A. & Van Duyne, R. P. Localized surface plasmon resonance spectroscopy and sensing. *Annu. Rev. Phys. Chem.* **58**, 267–297 (2007).

[36] Baer, M. *Beyond Born-Oppenheimer: electronic nonadiabatic coupling terms and conical intersections* (John Wiley & Sons, 2006).

[37] Varas, A., García-González, P., Feist, J., García-Vidal, F. & Rubio, A. Quantum plasmonics: from jellium models to ab initio calculations. *Nanophotonics* **5**, 409–426 (2016).

[38] Economou, E. N. *The physics of solids: essentials and beyond* (Springer Science & Business Media, 2010).

[39] D'Angelo, M., Chekhova, M. V. & Shih, Y. Two-photon diffraction and quantum lithography. *Physical review letters* **87**, 013602 (2001).

[40] Boto, A. N. *et al.* Quantum interferometric optical lithography: exploiting entanglement to beat the diffraction limit. *Physical Review Letters* **85**, 2733 (2000).

[41] Sun, L., Gibson, R. F., Gordaninejad, F. & Suhr, J. Energy absorption capability of nanocomposites: a review. *Composites Science and Technology* **69**, 2392–2409 (2009).

[42] Yablonovitch, E. Inhibited spontaneous emission in solid-state physics and electronics. *Physical review letters* **58**, 2059 (1987).

[43] Kleppner, D. Inhibited spontaneous emission. *Physical review letters* **47**, 233 (1981).

[44] Einstein, A. Strahlungs-emission und-absorption nach der quantentheorie. *Verh. Deutsch. Phys. Gesell.* **18**, 318–323 (1916).

[45] Koechner, W. *Solid-state laser engineering*, vol. 1 (Springer, 2013).

[46] Gould, R. G. *et al.* The laser, light amplification by stimulated emission of radiation. In *The Ann Arbor conference on optical pumping, the University of Michigan*, vol. 15, 92 (1959).

[47] Lamas-Linares, A., Howell, J. C. & Bouwmeester, D. Stimulated emission of polarization-entangled photons. *Nature* **412**, 887–890 (2001).

[48] Aguilar-Benitez, M. *et al.* Review of particle properties. *Phys. Lett., B* **170** (1986).

[49] Seidel, J., Grafström, S. & Eng, L. Stimulated emission of surface plasmons at the interface between a silver film and an optically pumped dye solution. *Physical review letters* **94**, 177401 (2005).

[50] Mendez, E. E. & von Klitzing, K. *Physics and applications of quantum wells and superlattices*, vol. 170 (Springer Science & Business Media, 2012).

[51] Bera, D., Qian, L., Tseng, T.-K. & Holloway, P. H. Quantum dots and their multimodal applications: a review. *Materials* **3**, 2260–2345 (2010).

[52] Czikklely, V., Forsterling, H. & Kuhn, H. Extended dipole model for aggregates of dye molecules. *Chemical Physics Letters* **6**, 207–210 (1970).

[53] Czikkely, V., Försterling, H. & Kuhn, H. Light absorption and structure of aggregates of dye molecules. *Chemical Physics Letters* **6**, 11–14 (1970).

[54] Högele, A., Galland, C., Winger, M. & Imamoğlu, A. Photon antibunching in the photoluminescence spectra of a single carbon nanotube. *Physical review letters* **100**, 217401 (2008).

[55] Rupasinghe, C., Zhu, W. & Premaratne, M. Spaser powered photothermal cancer therapy using graphene and carbon nanotubes. In *2014 IEEE Photonics Conference*, 16–17 (IEEE, 2014).

[56] Kudelski, A. & Wojtysiak, S. Silica-covered silver and gold nanoresonators for raman analysis of surfaces of various materials. *The Journal of Physical Chemistry C* **116**, 16167–16174 (2012).

[57] Della Valle, G., Søndergaard, T. & Bozhevolnyi, S. I. Plasmon-polariton nano-strip resonators: from visible to infra-red. *Optics express* **16**, 6867–6876 (2008).

[58] Kravets, V., Schedin, F., Kabashin, A. & Grigorenko, A. Sensitivity of collective plasmon modes of gold nanoresonators to local environment. *Optics letters* **35**, 956–958 (2010).

[59] Xu, T., Wu, Y.-K., Luo, X. & Guo, L. J. Plasmonic nanoresonators for high-resolution colour filtering and spectral imaging. *Nature communications* **1**, 1–5 (2010).

[60] Brar, V. W., Jang, M. S., Sherrott, M., Lopez, J. J. & Atwater, H. A. Highly confined tunable mid-infrared plasmonics in graphene nanoresonators. *Nano letters* **13**, 2541–2547 (2013).

[61] Lee, J., Wang, Z., He, K., Shan, J. & Feng, P. X.-L. High frequency mos2 nanomechanical resonators. *ACS nano* **7**, 6086–6091 (2013).

[62] Si, K. J. *et al.* Giant plasmene nanosheets, nanoribbons, and origami. *ACS nano* **8**, 11086–11093 (2014).

[63] Hill, M. T. *et al.* Lasing in metal-insulator-metal sub-wavelength plasmonic waveguides. *Optics express* **17**, 11107–11112 (2009).

[64] Li, D. & Stockman, M. I. Electric spaser in the extreme quantum limit. *Physical review letters* **110**, 106803 (2013).

[65] Liu, B., Zhu, W., Gunapala, S. D., Stockman, M. I. & Premaratne, M. Open resonator electric spaser. *ACS nano* **11**, 12573–12582 (2017).

[66] Gramotnev, D. K. & Bozhevolnyi, S. I. Plasmonics beyond the diffraction limit. *Nature photonics* **4**, 83 (2010).

[67] Oulton, R. F. Surface plasmon lasers: sources of nanoscopic light. *Materials Today* **15**, 26–34 (2012).

[68] Luo, Y., Fernandez-Dominguez, A., Wiener, A., Maier, S. A. & Pendry, J. Surface plasmons and nonlocality: a simple model. *Physical review letters* **111**, 093901 (2013).

[69] Myroshnychenko, V. *et al.* Modelling the optical response of gold nanoparticles. *Chemical Society Reviews* **37**, 1792–1805 (2008).

[70] Johnson, P. B. & Christy, R.-W. Optical constants of the noble metals. *Physical review B* **6**, 4370 (1972).

[71] Govyadinov, A. A., Panasyuk, G. Y., Schotland, J. C. & Markel, V. A. Theoretical and numerical investigation of the size-dependent optical effects in metal nanoparticles. *Physical Review B* **84**, 155461 (2011).

[72] Kelly, K. L., Coronado, E., Zhao, L. L. & Schatz, G. C. The optical properties of metal nanoparticles: the influence of size, shape, and dielectric environment (2003).

[73] Kumarasinghe, C., Premaratne, M. & Agrawal, G. P. Dielectric function of spherical dome shells with quantum size effects. *Optics express* **22**, 11966–11984 (2014).

[74] Gersten, J. & Nitzan, A. Electromagnetic theory of enhanced raman scattering by molecules adsorbed on rough surfaces. *The Journal of Chemical Physics* **73**, 3023–3037 (1980).

[75] Knight, M. W., Wu, Y., Lassiter, J. B., Nordlander, P. & Halas, N. J. Substrates matter: influence of an adjacent dielectric on an individual plasmonic nanoparticle. *Nano letters* **9**, 2188–2192 (2009).

[76] Sherry, L. J. *et al.* Localized surface plasmon resonance spectroscopy of single silver nanocubes. *Nano letters* **5**, 2034–2038 (2005).

[77] Barrow, S. J., Wei, X., Baldauf, J. S., Funston, A. M. & Mulvaney, P. The surface plasmon modes of self-assembled gold nanocrystals. *Nature communications* **3**, 1–9 (2012).

[78] Le, F. *et al.* Plasmons in the metallic nanoparticle- film system as a tunable impurity problem. *Nano Letters* **5**, 2009–2013 (2005).

[79] Kang, Z. *et al.* Plasmonic graded nano-disks as nano-optical conveyor belt. *Optics express* **22**, 19567–19572 (2014).

[80] Markus, A. *et al.* Simultaneous two-state lasing in quantum-dot lasers. *Applied Physics Letters* **82**, 1818–1820 (2003).

[81] Richter, M., Gegg, M., Theuerholz, T. S. & Knorr, A. Numerically exact solution of the many emitter–cavity laser problem: Application to the fully quantized spaser emission. *Physical Review B* **91**, 035306 (2015).

[82] Stockman, M. I. Spasers explained. *Nature Photonics* **2**, 327–329 (2008).

[83] Jayasekara, C., Premaratne, M., Gunapala, S. D. & Stockman, M. I. Is mos2 better for spasers than graphene? In *CLEO: QELS_Fundamental Science*, FTu1B–2 (Optical Society of America, 2016).

[84] Tran, S., DeGiovanni, P.-J., Piel, B. & Rai, P. Cancer nanomedicine: a review of recent success in drug delivery. *Clinical and translational medicine* **6**, 44 (2017).

[85] Tan, A. *et al.* Quantum dots and carbon nanotubes in oncology: a review on emerging theranostic applications in nanomedicine. *Nanomedicine* **6**, 1101–1114 (2011).

[86] Miao, L., Lin, C. M. & Huang, L. Stromal barriers and strategies for the delivery of nanomedicine to desmoplastic tumors. *Journal of Controlled Release* **219**, 192–204 (2015).

[87] Wagner, V., Dullaart, A., Bock, A.-K. & Zweck, A. The emerging nanomedicine landscape. *Nature biotechnology* **24**, 1211–1217 (2006).

[88] Wicki, A., Witzigmann, D., Balasubramanian, V. & Huwyler, J. Nanomedicine in cancer therapy: challenges, opportunities, and clinical applications. *Journal of controlled release* **200**, 138–157 (2015).

[89] Galanzha, E. I. *et al.* Spaser as a biological probe. *Nature communications* **8**, 15528 (2017).

[90] Chang-Claude, J. *et al.* Association between polymorphisms in the dna repair genes, xrcc1, ape1, and xpd and acute side effects of radiotherapy in breast cancer patients. *Clinical cancer research* **11**, 4802–4809 (2005).

[91] Brannon-Peppas, L. & Blanchette, J. O. Nanoparticle and targeted systems for cancer therapy. *Advanced drug delivery reviews* **56**, 1649–1659 (2004).

[92] Harrow, A. W. & Montanaro, A. Quantum computational supremacy. *Nature* **549**, 203–209 (2017).

[93] Xie, Z. *et al.* Plasmonic nanolithography: a review. *Plasmonics* **6**, 565 (2011).

[94] Hell, S. W. Toward fluorescence nanoscopy. *Nature biotechnology* **21**, 1347–1355 (2003).

[95] Sahl, S. J., Hell, S. W. & Jakobs, S. Fluorescence nanoscopy in cell biology. *Nature reviews Molecular cell biology* **18**, 685 (2017).

[96] Khurgin, J. B. & Sun, G. How small can "nano" be in a "nanolaser"? *Nanophotonics* **1**, 3–8 (2012).

[97] Berman, O. L., Kezerashvili, R. Y. & Lozovik, Y. E. Graphene nanoribbon based spaser. *Physical Review B* **88**, 235424 (2013).

[98] Vinogradov, A. P., Andrianov, E. S., Pukhov, A. A., Dorofeenko, A. V. & Lisyansky, A. A. Quantum plasmonics of metamaterials: loss compensation using spasers. *Physics-Uspekhi* **55**, 1046 (2012).

[99] Kobayashi, T., Kawaguchi, H. & Furukawa, Y. Lasing characteristics of very narrow planar stripe lasers. *Japanese Journal of Applied Physics* **16**, 601 (1977).

[100] Lang, R. & Kobayashi, K. External optical feedback effects on semiconductor injection laser properties. *IEEE journal of Quantum Electronics* **16**, 347–355 (1980).

[101] Hapuarachchi, H. *et al.* Cavity qed analysis of an exciton-plasmon hybrid molecule via the generalized nonlocal optical response method. *Physical Review B* **95**, 245419 (2017).

[102] Hapuarachchi, H., Mallawaarachchi, S., Hattori, H. T., Zhu, W. & Premaratne, M. Optoelectronic figure of merit of a metal nanoparticle—quantum dot (mnp-qd) hybrid molecule for assessing its suitability for sensing applications. *Journal of Physics: Condensed Matter* **30**, 054006 (2018).

[103] Hapuarachchi, H., Gunapala, S. D., Bao, Q., Stockman, M. I. & Premaratne, M. Exciton behavior under the influence of metal nanoparticle near fields: Significance of nonlocal effects. *Physical Review B* **98**, 115430 (2018).

[104] Eichhorn, M. Quasi-three-level solid-state lasers in the near and mid infrared based on trivalent rare earth ions. *Applied Physics B* **93**, 269 (2008).

[105] Qiu, J. *et al.* Femtosecond laser-induced three-dimensional bright and long-lasting phosphorescence inside calcium aluminosilicate glasses doped with rare earth ions. *Applied physics letters* **73**, 1763–1765 (1998).

[106] Jha, P. K., Wang, Y., Ren, X. & Zhang, X. Quantum-coherence-enhanced transient surface plasmon lasing. *Journal of Optics* **19**, 054002 (2017).

[107] Shahbazyan, T. V. Mode volume, energy transfer, and spaser threshold in plasmonic systems with gain. *ACS Photonics* **4**, 1003–1008 (2017).

[108] Trivedi, D. J., Wang, D., Odom, T. W. & Schatz, G. C. Model for describing plasmonic nanolasers using maxwell-liouville equations with finite-difference time-domain calculations. *Physical Review A* **96**, 053825 (2017).

[109] Breuer, H.-P., Petruccione, F. *et al. The theory of open quantum systems* (Oxford University Press on Demand, 2002).

[110] Carmichael, H. J. *Statistical methods in quantum optics 2: Non-classical fields* (Springer Science & Business Media, 2009).

[111] Nilius, N., Ernst, N. & Freund, H.-J. Photon emission spectroscopy of individual oxide-supported silver clusters in a scanning tunneling microscope. *Physical review letters* **84**, 3994 (2000).

[112] Kolwas, K. & Derkachova, A. Plasmonic abilities of gold and silver spherical nanoantennas in terms of size dependent multipolar resonance frequencies and plasmon damping rates. *Opto-Electronics Review* **18**, 429–437 (2010).

[113] Kumarapperuma, L., Premaratne, M., Jha, P. K., Stockman, M. I. & Agrawal, G. P. Complete characterization of the spasing (ll) curve of a three-level quantum coherence enhanced spaser for design optimization. *Applied Physics Letters* **112**, 201108 (2018).

[114] Scully, M. O., Zhu, S.-Y. & Gavrielides, A. Degenerate quantum-beat laser: Lasing without inversion and inversion without lasing. *Physical review letters* **62**, 2813 (1989).

[115] Jayasekara, C., Premaratne, M., Stockman, M. I. & Gunapala, S. D. Multimode analysis of highly tunable, quantum cascade powered, circular graphene spaser. *Journal of Applied Physics* **118**, 173101 (2015).

[116] Lorin, E., Chelkowski, S. & Bandrauk, A. A numerical maxwell–schrödinger model for intense laser–matter interaction and propagation. *Computer Physics Communications* **177**, 908–932 (2007).

[117] Zurek, W. H. Decoherence, einselection, and the quantum origins of the classical. *Reviews of modern physics* **75**, 715 (2003).

[118] Mallawaarachchi, S., Premaratne, M. & Maini, P. K. Superradiant cancer hyperthermia using a buckyball assembly of quantum dot emitters. *IEEE Journal of Selected Topics in Quantum Electronics* **25**, 1–8 (2018).

[119] Liu, X., Zhang, R. & Zhang, Z. Near-field thermal radiation between hyperbolic metamaterials: Graphite and carbon nanotubes. *Applied Physics Letters* **103**, 213102 (2013).

[120] Kholmanov, I. N. *et al.* Improved electrical conductivity of graphene films integrated with metal nanowires. *Nano letters* **12**, 5679–5683 (2012).

[121] Zhang, P. *et al.* Fracture toughness of graphene. *Nature communications* **5**, 3782 (2014).

[122] Balandin, A. A. Thermal properties of graphene and nanostructured carbon materials. *Nature materials* **10**, 569–581 (2011).

[123] Thongrattanasiri, S., Manjavacas, A. & Garcia de Abajo, F. J. Quantum finite-size effects in graphene plasmons. *Acs Nano* **6**, 1766–1775 (2012).

[124] Rupasinghe, C., Rukhlenko, I. D. & Premaratne, M. Spaser made of graphene and carbon nanotubes. *ACS Nano* **8**, 2431–2438 (2014).

[125] Senevirathne, V. *et al.* Scattering characteristics of an exciton-plasmon nanohybrid made by coupling a monolayer graphene nanoflake to a carbon nanotube. *Journal of Physics: Condensed Matter* **31**, 085302 (2019).

[126] Senevirathne, V. & Premaratne, M. Comparison of the permittivity sensing capabilities of graphene-based nanohybrids and metal nanoparticle-based nanohybrids. In *2019 IEEE 19th International Conference on Nanotechnology (IEEE-NANO)*, 302–305 (IEEE, 2019).

[127] Andrianov, E., Pukhov, A., Dorofeenko, A., Vinogradov, A. & Lisyansky, A. Stationary behavior of a chain of interacting spasers. *Physical Review B* **85**, 165419 (2012).

[128] Dorofeenko, A. V. *et al.* Steady state superradiance of a 2d-spaser array. *Optics express* **21**, 14539–14547 (2013).

[129] Voronine, D. V., Huo, W. & Scully, M. Ultrafast dynamics of surface plasmon nanolasers with quantum coherence and external plasmonic feedback. *Journal of Optics* **16**, 114013 (2014).

[130] Berini, P., Charbonneau, R., Lahoud, N. & Mattiussi, G. Characterization of long-range surface-plasmon-polariton waveguides. *Journal of Applied Physics* **98**, 043109 (2005).

[131] Holmgaard, T. & Bozhevolnyi, S. I. Theoretical analysis of dielectric-loaded surface plasmon-polariton waveguides. *Physical Review B* **75**, 245405 (2007).

[132] Kristanz, G. V., Arnold, N., Kildishev, A. V. & Klar, T. A. Power balance and temperature in optically pumped spasers and nanolasers. *ACS photonics* **5**, 3695–3703 (2018).

[133] Kumarapperuma, L. & Premaratne, M. Quantum coherence enhanced graphene spaser. In *Integrated Photonics Research, Silicon and Nanophotonics*, IW2A–5 (Optical Society of America, 2019).

[134] Chlouverakis, K. E. & Adams, M. J. Stability maps of injection-locked laser diodes using the largest lyapunov exponent. *Optics communications* **216**, 405–412 (2003).

[135] Babin, S. *et al.* Relative intensity noise in cascaded-raman fiber lasers. *IEEE Photonics technology letters* **17**, 2553–2555 (2005).

[136] Lang, R. Injection locking properties of a semiconductor laser. *IEEE Journal of Quantum Electronics* **18**, 976–983 (1982).

[137] Khurgin, J. B. & Sun, G. Comparative analysis of spasers, vertical-cavity surface-emitting lasers and surface-plasmon-emitting diodes. *Nature Photonics* **8**, 468 (2014).

[138] Chen, H.-Z. *et al.* Imaging the dark emission of spasers. *Science advances* **3**, e1601962 (2017).

[139] Maurya, J., Prajapati, Y. & Tripathi, R. Effect of molybdenum disulfide layer on surface plasmon resonance biosensor for the detection of bacteria. *Silicon* **10**, 245–256 (2018).

[140] Correas-Serrano, D., Gomez-Diaz, J., Melcon, A. A. & Alù, A. Black phosphorus plasmonics: anisotropic elliptical propagation and nonlocality-induced canalization. *Journal of Optics* **18**, 104006 (2016).

[141] Moscatelli, A. Plasmonics: the aluminium rush. *Nature nanotechnology* **7**, 778 (2012).

[142] Knight, M. W. *et al.* Aluminum for plasmonics. *ACS nano* **8**, 834–840 (2014).